ANALYSIS OF THE IMPACT OF FLOW ON THE UNDERWATER ACOUSTIC CHANNEL

by

Jeff MacDonald

Submitted in partial fulfillment of the requirements
for the degree of Master of Applied Science

at

Dalhousie University
Halifax, Nova Scotia
December 2021

Dedicated to my Family

Table of Contents

List of Tables

List of Figures

Abstract

Reliable and power efficient underwater communication systems that can adapt to the medium's changing nature can be designed with knowledge of the physical underwater environment. This thesis discusses a stochastic model for an underwater acoustic channel that takes into consideration the effects of mean flow and turbulence on the acoustic signal in environments subject to some of the highest tides in the world. The model, relying fundamentally on ray tracing, generates an ensemble of time-varying channel characteristics by capturing the effect of known environmental changes, including the effective perturbation of the sound speed in the medium through mean and turbulent flow. The model is used to extract the channel characteristics such as channel gain, delay spread, Doppler spread, and propagation delay. By validating simulation results with real measurements taken in the Bay of Fundy, it is demonstrated that the mean flow has significant impact on various channel characteristics.

Acknowledgements

I thank JASCO Applied Sciences for providing the acoustic data from Grand Passage, Nova Scotia; I thank Mitacs for help providing the connection between post-secondary institutions and industry. I thank both these partners for financial support.

Chapter 1

Introduction

1.1 Background

The ocean is a critical resource to human kind and it must be managed carefully to ensure sustainability. As the population increases, food security is becoming a major global challenge. There is an increasing reliance on the ocean to provide a reliable food source for the ever increasing population which is expected to reach 10 billion by 2050 [3]. In 2018, global fisheries, and aquaculture production totalled 179 million tons, of which 87% of total fish production was used for human consumption. In the same year, the global fish trade amounted to $151 billion. Even basic food products like peanut butter and soymilk use ingredients extracted from the ocean. Also some medicines used in the treatment of cancer, Alzheimer's and heart disease rely on the ocean environment for their production [4]. The preponderance of scientific evidence indicates we are facing a significant climate change challenge replacing fossil fuels with sustainable green energy. The ocean has the potential to provide sustainable green energy in the form of stored thermal energy as well as mechanical energy which can come from waves and tidal flows [5].

With the importance of finding alternative sustainable green energy sources, a number of techniques exploiting tidal areas have been attempted in recent years. Tidal energy has benefits over other green renewable energy sources such as wind and solar. Tidal energy is significantly more efficient than wind energy due to the density of water, a measure of mass per unit volume, and more efficient than solar energy due to its high conversion efficiency of roughly 80% [6]. However, the cost of equipment and its rapid deterioration in seawater have prevented a widespread deployment of infrastructure extracting tidal energy. Despite these challenges, companies such as Ocean Power Technologies are developing methods to generate power from wave energy [7], while other companies are researching power generation taking advantage of the significant water flow associated with unique tidal areas such as the Bay of Fundy. These are only examples of the increasing activity within the ocean environment leading to increases in equipment, machinery and technology deployed. Considering the

anticipated increase in activities, an efficient and effective means to monitor the ocean environment and even enhance the interoperability of systems and processes functioning within the environment would be very beneficial.

With some of the highest tides in the world, the Bay of Fundy is a key location to generate electricity from tides. The Minas Basin, an inlet of the Bay of Fundy, offers tremendous energy opportunities [8], while tidal platforms have been successfully installed near Briar Island. With these high tides come very high-flow rates. To take advantage of this energy, it requires the installation of power generating turbines, which means infrastructure will be deployed and monitored under the sea surface.

In order to deploy costly infrastructure below the sea surface, it is important that it is monitored. Cabled platforms can be deployed; however, the cost can be high, with an inherent risk of damage and or failure. Laying subsea cables to provide control and monitoring between platforms can be disruptive to the marine environment. Also, subsea cables are easily damaged in regions of high velocity flow, as well as in the inter-tidal zone, where surface waves subject them to large forces. As such, wireless communication is an attractive option to monitor underwater infrastructure due to its low cost, efficient set up, and reduced disruption to marine life.

In contrast to wireless communications through the atmosphere where electromagnetic energy is used to transmit information, in the ocean it is more common to communicate using acoustic sources, and acoustic propagation has been identified to be an attractive method for wireless communications underwater [9]. In fact, acoustic signals propagate significantly further than electromagnetic signals underwater; therefore, acoustics are used as the primary method for communication systems underwater. Properly designed and deployed, underwater acoustic communication systems could provide benefits in supporting commercial and industrial activities within the ocean environment and could be used as a technology to monitor the overall health of the marine environment.

As shown in Figure 1.1, a simple acoustic communication system can enable digital data transmission between two remote nodes. The transmitter converts user information, and modulates it on a carrier. The digital signal at the transmitter is converted to an analog signal using a digital to analog converter (DAC), amplified and typically applied to a piezo-electric transducer. The transducer converts the electric energy to mechanical pressure waves which propagate through the water. When the transmitted signal, in the form of these

pressure waves, arrives at the receiving hydrophone, it is distorted by the propagation media and combined with ambient noise. The receiving hydrophone converts the pressure waves into an electrical signal. At the output of the hydrophone, a low-noise amplifier conditions the signal, which is converted to a digital signal using an analog-to-digital-converter (ADC). The output of the ADC is further processed digitally to mitigate the distortion and decode the data.

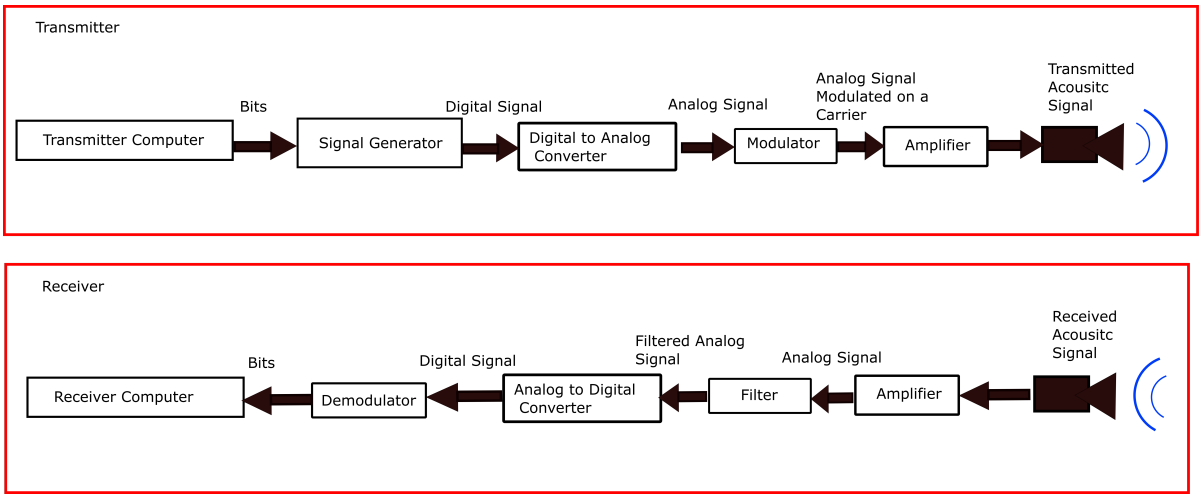

Figure 1.1: Acoustic transmitter and receiver block diagram

Underwater acoustic modems are commercially available with a range of designs and specifications. With a fixed transmit power, the achievable data throughput depends on the transmit frequency and on the required transmission range. According to [1], the data rate is high at lower ranges, upwards of 40 kbps at 100 meters and low at further ranges at around 1 kbps at 89 km. Table 1.1 contains a list of typical commercial modems and some of their operating characteristics. As an example, in Table 1.1, the Teledyne Benthos model ATM-916-MF1 is specified to have a range of 6000 meters and can transmit a maximum bit rate of 15 kbps in a frequency band between 16 kHz and 21 kHz. In Table 1.1, each modem is optimized for different conditions by the manufacturers. [1]

The limitations of acoustic modems depend on the transducer characteristics, on the available power at the nodes, and on the characteristics of the acoustic propagation link. Lower frequencies travel significantly greater distances than higher frequencies because of the lower acoustic absorption of sea water; however, they have a lower available bandwidth. In fact, the transmit distance constrains the maximum achievable bit rate. Additionally, the acoustic communication link, is affected by environmental factors that can degrade the

Table 1.1: Acoustic modems presented by Stojanovic and Beaujean [1]

Product Name	**Maximum Bit Rate (bps)**	**Range (m)**	**Frequency band (kHz)**
Teledyne Benthos ATM-916-MF1 [10]	15360	6000	16-21
WHOI Micromodem [11]	5400	3000	22.5-27.5
Linkquest UWM 1000 [12]	7000	1200	27-45
Evologics S2C R 48/78 [13]	31200	2000	48-78
Sercel MATS 3G 34 kHz [14]	24600	5000	30-39
Tritech Micron Data Modem [15]	40	500	20-28

throughput. Therefore, it is important to analyze and measure the acoustic channel characteristics to assess the impact on the communication link and mitigate its impact. This is particularly true in high-flow shallow environments, that significantly complicate the physics of propagation. As such, a thorough analysis of the communication link can serve to develop signal processing techniques to mitigate distortion.

With advances in artificial intelligence, understanding how the transmitted signal is affected as it propagates through the acoustic channel can provide an opportunity to create reconfigurable modems that adapt to the conditions measured between the transmitter and the receiver. For this purpose, it is possible to monitor the physical conditions such as water temperature, salinity, flow speed, depth, and ambient noise over time using heterogeneously distributed sensors. In fact, monitoring the environment can provide insight about the acoustic propagation media.

Distortion in the acoustic propagation channel changes the form or shape of the signal, and various characteristics of the acoustic channel create impairments which degrade the acoustic signal. As the signal propagates through space, wave propagation theory predicts an attenuation in power. In the ocean, absorption is mainly due to the loss of acoustic energy into chemical reactions related to the salts in seawater. Because of absorption in the ocean, the channel bandwidth is very limited and for distances above 1 km, the maximum available bandwidth is on the order of 10 kHz. Due to the low speed of sound in sea water (approximately 1480 m/sec in the Atlantic), the long latency between a transmitter and receiver also creates additional challenges in the transmission of messages. Furthermore, the signal is subject to reflections from the surface and bottom. As such, the signal arrives at the receiver, through multiple paths each with different intensities and delays. Mobility

of the nodes, as well as currents and surface motion introduce a propagation media with characteristics that vary with time. Noise from the environment will also add random or unwanted signals to altar the transmitted signal's original state. Environmental noise can combine with the acoustic signal which creates reliability issues and affects the throughput. Overall, the time-varying multipath fading nature of the underwater acoustic channel makes it a challenging medium for wireless communication, and its characteristics are influenced by its environmental conditions.

Time varying latency has a significant effect on the communication link. Every communication link regardless of the transmission medium has some measure of latency. Time varying latency in underwater communication links has negative effects on time synchronization. The transmitter and receiver clocks need to be synchronized to a common event, and relative to an absolute frequency or there will be skew. Currently phase-locked loops and linear regression are used to correct the skew of the local clock frequency. In addition, time varying latency also creates fading that needs to be compensated for [16]. As an example, a 10 km link with a sound speed of 1480 meters per second, would introduce 6.7 seconds of delay. Latency due to the hardware is relatively fixed, where latency varies significantly with the length of the communication link, and to some degree with changes in sound speed which is affected by temperature, salinity and depth. Where the objective of a communication link is to transmit information across the link, it is clear that latency has a significant effect on throughput. Having little control over the properties that affect sound speed, to maximize throughput, keeping the links as short as possible, and maximizing the bandwidth are the key options.

Having the ability to predict the performance of a specific communication link based on the known characteristics of the acoustic channel would be extremely beneficial. Knowledge of the physical environment and acoustic channel fading characteristics can be used to design reliable and power-efficient underwater communication systems that can adapt to the underwater acoustic transmission medium's changing nature. There are various techniques used to improve the communication link. Analysing and improving the signal at the receiver is important in understanding why the transmitted signal has been altered as it arrives at the receiver. Therefore, estimating, and adapting to the acoustic channel is important in understanding what happens to the signal. Current estimation techniques include multiple

input, multiple output orthogonal frequency division multiplexing (MIMO-OFDM) consisting of multiple transmitters and multiple receivers. A review in [17], discusses the benefits of MIMO-OFDM to improve the bandwidth, efficiency and performance of underwater communications. MIMO-OFDM is also used for channel estimation, using a non-linear least squares method from the multiple channel estimations. According to [18], OFDM reduces the receiver complexity, and can help improve data rates at a low signal to noise ratio (SNR). The reliability of OFDM can be improved using a Doppler compensation discussed in [19]. The Doppler spread can degrade the communication link; however, using a time-scaling factor over the channel and time-varying resampling, this can be compensated for.

Another technique uses a decision-feedback equalizer with an adaptive channel estimator [20]. The technique uses the channel components consisting of a delay span shorter than the multipath spread. This helps cancel intersymbol interference and achieve spatial diversity gain. In [21], Stojanovic discusses a statistical channel model using frequency-dependent attenuation, various reflections, with the added random displacements from small scale environmental effects. This includes signal scattering, and motion-induced Doppler shifting that affects the channel.

Subject to time-varying propagation conditions, tidal environments create additional challenges. In tidal environments, the variables that affect the sound speed can be constantly in flux with significant flow rates that change with the incoming and outgoing tide. Turbulence is also a factor where there may be areas of turbulence on the incoming tide that may change with the outgoing tide. In particular, the Bay of Fundy with its extreme tides exaggerates these challenges. Grand Passage, the study area for this project, is at 20 meters depth and is a typically shallow area within the Bay of Fundy that experiences these high tide cycles creating high-flows for several hours and causing significant turbulence. The effect of flows and turbulence in the ocean are not accurately represented in existing acoustic simulation tools. As explained in [22], the velocity of the medium affects the velocity of the acoustic signal propagation through advection, which is defined as the transport of matter, heat, or in this case the acoustic signal, from one place to another through fluid flow, and depends on the water velocity.

In Figure 1.2, the propagation environment is conceptually represented in a shallow area with high-flow, representative of an area in which tidal turbines are installed. From the transmitter, the acoustic signal is shown to arrive at the receiver through two paths: a direct

path, and a surface reflection. The water flow induced by tides between the transmitter and receiver varies as a function of time and as a function of tide height [8, 23]. Turbulence is also created because of the variable bathymetry, large objects in the water, and the geographical characteristics of the littoral zone [24, 23]. In this work, turbulence is modelled using a random variable with correlation as a function of space. The turbulent component of the flow is also assumed to have a homogeneous correlation function between the source and receiver, and varies with time and tide height. The properties of the turbulence are linked with the magnitude of the tidally driven mean flow in the channel.

Note that turbulence and fluid flow in general creates flow noise [25], a unique type of noise that is apparent on sensors at low frequency. Specifically, the flow noise bandwidth, shape and magnitude are related to the flow speed and shape of the hydrophone. Flow noise can also mask the signal of interest degrading the communication link. In a fluid, turbulence is when the fluid has chaotic changes in its flow velocity and pressure. Turbulence can consist of unstable eddies that range from large scale turbulence to smaller microscopic eddies that interact with each other. Tidal flows can generate noise from sound radiated by turbulence, and from psuedo-noise, generated on the transducer by the turbulent pressure fluctuations in the flow [26].

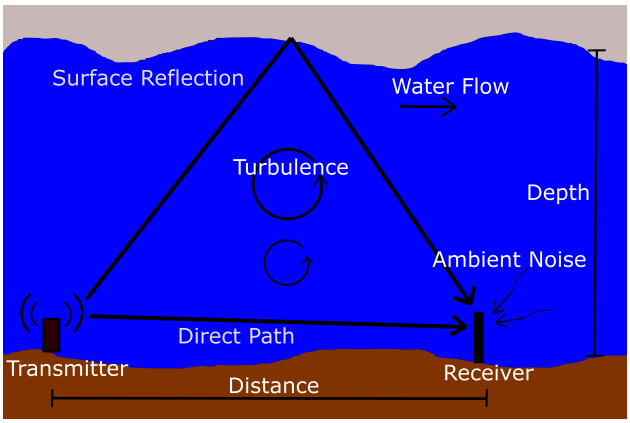

Figure 1.2: Conceptual representation of propagation media in a shallow, high-flow environment.

To mitigate impairments in high-flow environments, the impact of flow noise has been studied [25]. However, it is not clear how the time-varying channel characteristics in tidal areas affect the actual propagation channel between the transmitter and receiver. For this purpose, it is important to develop a model that is representative of propagation behaviour.

Complementary work on modelling the underwater acoustic channel includes the Bellhop physics based model [27, 28] and Stojanovic's stochastic model to represent small-scale variations [29]. In contrast, empirical models, such as those described in [30], are unique to a specific environment. To model time-variance, in [29] the underwater acoustic channel is represented using frequency-dependent large-scale attenuation, and is combined with a set of stochastic processes to model time-varying random local displacements in a multipath environment. This includes scattering of the acoustic signal from the time varying surface, and Doppler shift due to potential node mobility from the moving medium. The model also takes into account different physical parameters, including unintentional motion of the nodes and surface roughness. However, the effect of flow is not included.

In this thesis, different characteristics of the propagation channel in high-flow environments will be discussed. Specifically, the time-varying latency and relevant channel parameters will be analyzed, including the Doppler spread, the amplitude variation, and the multipath characteristics. The tidal environment used to validate the model is Grand Passage, in Nova Scotia, an area that has been identified to allow tidal energy extraction. For this purpose, acoustic data from a 35 day sea trial to characterize the acoustic channel will be analyzed.

1.2 Research Objectives

The goal of this thesis is to obtain an understanding of physical behaviour of the acoustic propagation in a high-flow turbulent environment. Due to significant water motion, a model of acoustic propagation through turbulent media was developed, and builds on a ray tracing algorithm [28]. In this work, the model is enhanced to account for variable sound speeds as a function of range, to represent the impact of advection of the acoustic signal by the mean flow and turbulence on the propagation delay characteristics, and effectively the variations on channel amplitude and on delay spread. The model developed is compared to a model relying on a stochastic process that represents the effect of tide height, and surface variation. The simulation results are also validated using measured channel characteristics for a deployment in a tidal channel, at Grand Passage in the Bay of Fundy.

The importance of this research is based on the increasing operations and deployment of equipment in tidal environments. Tidal environments around the world are of interest to power companies for generating electricity from large tidal flows. These systems could

include underwater turbines, which would need to be monitored, carrying remotely networked sensors. Wireless communications is favorable, over laying subsea cables because of cost. As an example, underwater turbine systems need to detect nearby animals and shut down if there is a possible conflict.

In modern communication systems models, the impact of flow and turbulence on the communication link is not fully understood. Large tidal flows create significant turbulence and flow noise at the hydrophones. To improve modern underwater communication systems, the effects of flow and turbulence on performance requires more research.

1.3 Organization of Thesis

This thesis is organised as follows: In Chapter 2, the fundamental concepts on the physics of acoustic propagation are described. Next, the Grand Passage high-flow environment in which the experiment was conducted is discussed. This includes a description of the location of the experiment, the acoustic and environmental data collected, and an analysis of the environmental conditions during the measurement period between September and October 2018.

In Chapter 3, the methods to calculate the channel characteristics are explained, and the results are shown. The acoustic data over 35 days are extracted, and analyzed. First the channel characteristics are obtained, and this includes determining the channel gain, delay spread, Doppler spread, and propagation delay. In addition, this chapter shows an extrapolation of recorded flow speeds and pressure data. Due to the hardware limits of the flow and pressure recording instrument, there are only 14 days of flow and pressure data compared with 35 days of acoustic data. Therefore, the flow speeds and pressure are extrapolated over the remaining 21 days.

In Chapter 4, the developed stochastic channel characteristics model is presented. An introduction to the ray tracing algorithm is discussed, followed by modelling the channel gain and delay spread in the presence of tides. The effect of turbulence on the acoustic propagation is modelled as an environment with a constant sound speed with range dependent perturbations. The sound speed perturbations have characteristic length and speed scales chosen to replicate the turbulent advection effect and are determined from physical measurements of the flow. A statistical analysis of various arrival times are computed with the help of the ray tracing algorithm Bellhop to determine the variability of the signal travel time

along multiple paths. The signal propagation delay variability is modelled and presented with differing turbulent lengths, using different range dependent sound speeds.

In Chapter 5, the channel characteristics such as transmission loss, delay spread, Doppler spread and propagation delay are analyzed from the data collected in Grand Passage. The data are compared to the stochastic model presented in the previous chapter. Finally in Chapter 6, conclusions are presented.

Chapter 2

The Theory of Acoustic Propagation in High Flow Environments

In this chapter, relevant concepts in underwater acoustics are presented and the experiment site and data collection details are discussed. Specifically; in Section 2.1, the theory of acoustic propagation in high-flow and turbulent environments is discussed; in Section 2.2, an experiment carried out in Grand Passage will be described; finally, in Section 2.3, a summary of this chapter is provided.

2.1 Fundamental Physics of Acoustics

Acoustic communication performance is hard to predict, particularly with an environment that is subject to high-flows, turbulence, and changes in water pressure. As such, it is important to review the physical properties of an acoustic signal travelling through an underwater environment, that can affect the performance of the communication link. This section will describe the fundamental theory of acoustic propagation. Specifically; in Section 2.1.1, models of transmission loss are presented; in Section 2.1.2, the propagation delay of the acoustic signal is described; in Section 2.1.3, the figure of merit to quantify the multipath characteristics of the channel is provided; in Section 2.1.4, the Doppler shift and spread induced by flow and mobile boundaries are described; in Section 2.1.5, the effect of surface waves, mean flow and turbulence are discussed; in Section 2.1.6, the ambient noise properties in shallow environments subject to flow are summarily reviewed.

2.1.1 Transmission Loss

The objective of this section is to determine the transmission loss of an acoustic signal between a transmitter and receiver. Transmission loss is a reduction in signal intensity as it propagates through the underwater environment. Transmission loss is represented as the logarithmic ratio of the initial sound intensity referenced at a one meter distance from the transmitter, I_o and the intensity at a depth z, and a range, r from the transmitter. The

intensity at this point is represented as $I(r, z)$, with units of watts per square meter (W/m^2). The transmission loss is expressed in decibel units as

$$\mathrm{TL} = 10 \log \frac{I(r, z)}{I_0}. \tag{2.1}$$

Alternatively, transmission loss of an acoustic signal can also be calculated in terms of pressure that is proportional to the square root of the intensity, such that

$$\mathrm{TL} = 20 \log \frac{p(r, z)}{p_0}, \tag{2.2}$$

where p_o is the acoustic pressure at the transmitter, and $p(r, z)$ is the acoustic pressure at a depth z and a range r, expressed as in units of pascals (Pa).

A simple model of transmission loss is one that considers only the geometric spreading of the acoustic wave. Two types of geometric spreading will be presented: spherical spreading and cylindrical spreading.

Spherical spreading transmission loss is used when the energy of the acoustic signal radiates away from a source equally in all directions in an unbounded medium. The energy radiating from a point source in a homogeneous medium is equally distributed over the surface of a sphere [31]. The intensity is inversely proportional to the surface of the spherical wave, $I \propto 1/(4\pi R^2)$, where R is the radius of the acoustic sphere as shown in Figure 2.1. Spherical spreading transmission loss can be represented as

$$\mathrm{TL} = 20 \log_{10} R, \tag{2.3}$$

where R is the range between the transmitter and receiver and the units are in dB re 1m.

In shallow water with a relatively flat seabed, sound is approximately distributed uniformly over the surface of a cylinder having a radius equal to the range R and a height D equal to the depth of the ocean. The transmission loss is estimated using cylindrical spreading where the medium has parallel top and bottom boundaries, also referred to as a waveguide. The intensity of the signal in the far-field is related to the surface of a cylinder, $I \propto 1/(2\pi RD)$, as shown in Figure 2.1. Cylindrical spreading transmission loss is expressed as

$$\mathrm{TL} = 10 \log_{10} R, \tag{2.4}$$

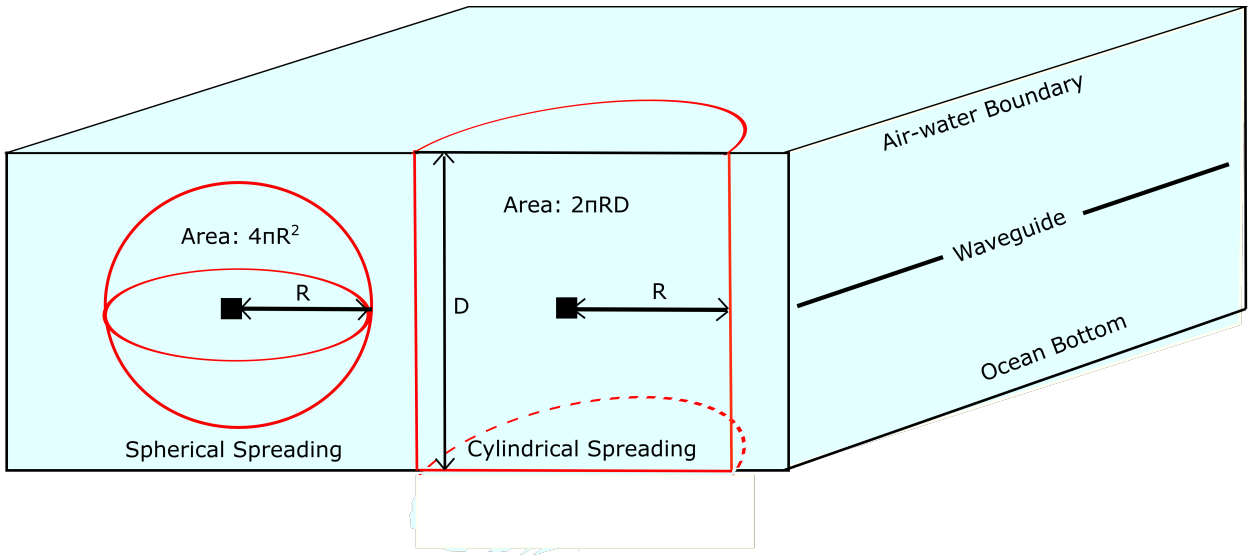

Figure 2.1: Spherical and cylindrical spreading transmission loss

where once again, R is the distance from the source to a point in the far-field.

The transmission loss is also dependent on attenuation, and absorption. Attenuation is the continuous loss of acoustic energy as it propagates through a medium, where as absorption depends on the molecular loss. This factor, denoted by $\alpha(f)$, is known as the absorption coefficient, expressed in units of dB/km. The attenuation is frequency dependent and depends on the salinity, temperature, and pressure of sea water. According to Urick [31], this attenuation coefficient combined with spherical spreading transmission loss provides a reasonable estimate of transmission loss under various ocean conditions. The transmission loss with attenuation related to the frequency, f in kilohertz is expressed as

$$\mathrm{TL} = 20\log_{10} R + \alpha(f)\left(\frac{R}{1000}\right), \tag{2.5}$$

where R is the propagation distance in meters, and $\alpha(f)$ is the attenuation coefficient in dB/km. According to Urick [31], the attenuation coefficient $\alpha(f)$ is primarily due to absorption and is related to the frequency, f, in kilohertz such that

$$\alpha(f) = \left(\frac{0.1f^2}{1+f^2}\right) + \left(\frac{40f^2}{4100+f^2}\right) + 2.75\times 10^{-4} f^2. \tag{2.6}$$

Shallow ocean channels are typically modelled as a waveguide with the air-water interface as the top boundary and the bottom of the channel as the bottom boundary. In this situation, the transmission loss can be estimated with spherical spreading to the upper and lower

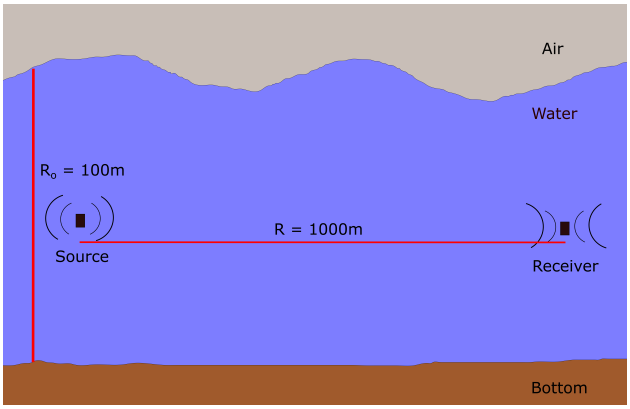

Figure 2.2: Transmission loss example. The depth of the wave guide, R_o is 100 meters. The receiver, R is 1000 meters away from the source. The frequency, f of the signal is 8 kHz.

boundaries where it then transitions to cylindrical spreading. If R is the total range in meters, and R_o is the transition range between spherical and cylindrical spreading expressed in meters, then the transmission loss is written as

$$\mathrm{TL}' = 20\log_{10} R_o + A\log_{10}\left(\frac{R}{R_o}\right) + \alpha(f)\left(\frac{R}{1000}\right). \tag{2.7}$$

Setting $A = 10$ results in the transition from spherical spreading to cylindrical spreading. When $R < R_o$, the transmission loss can be estimated using Equation (2.5), which only considers spherical spreading and attenuation. However, when $R \geq R_o$, Equation (2.7) is valid and the transmission loss is estimated with spherical spreading for the transition distance added with cylindrical spreading and attenuation losses for the remaining distance [28].

In this thesis, the frequency of the acoustic signals to be discussed range from 8 kHz to 16 kHz, with propagation distances up to one kilometer. At these frequencies and distances, the last frequency-dependent term in Equation (2.7) is quite small, and can be neglected when estimating the transmission losses. For example, assume a point source in a homogeneous shallow waveguide at a frequency of 8 kHz, with a length of 1 km. The first 100 m is spherical spreading followed by cylindrical spreading for the remaining distance. The transmission loss using Equations (2.7), and (2.6), is 40 dB+10 dB+0.8 dB = 50.8 dB. Without the frequency dependent term, the estimate is 50 dB; therefore, in this work, it is neglected when estimating the transmission loss. This transmission loss example is shown in Figure 2.2. As can be seen, transmission loss between the transmitter and receiver impacts the signal strength, and can affect sound speed depending on the environmental conditions.

The sound speed in seawater is determined by the salinity, temperature and pressure of the water through which sound is propagating. Sound speed increases with the pressure of the medium, and the pressure of the water increases with depth. However, near the ocean surface, the impact of temperature and salinity on the speed of sound is greater than the impact of pressure, causing the speed of sound to decrease before increasing with depth as a result of decreasing temperature. The combined effect of the decreasing temperature and the increasing pressure with depth forms a sound speed gradient that generates an acoustic duct. An example of a shallow water sound speed profile (SSP) is shown in Figure 2.3a, where the vertical axis is the ocean depth in meters, and the horizontal axis is the sound speed in meters per second. The duct is seen at a depth from 25 to 75 meters, where the SSP has a minimum.

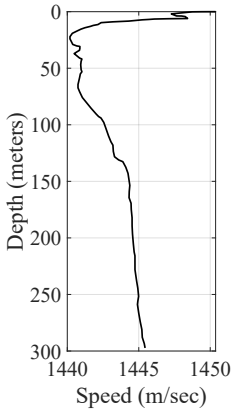

(a) Arctic sound speed profile

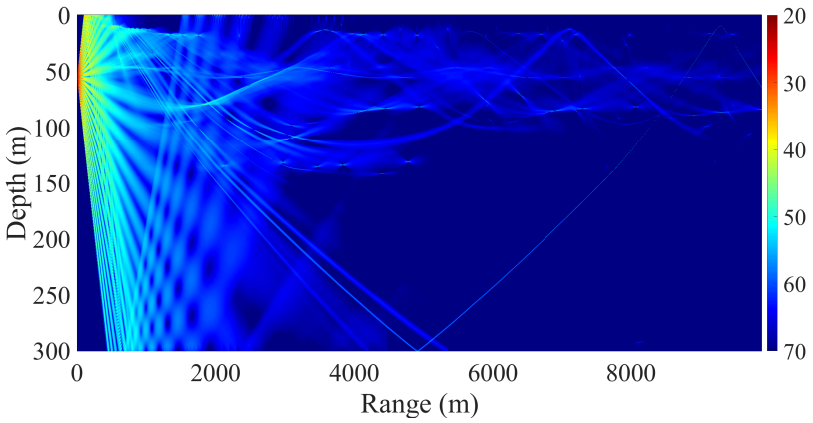

(b) Transmission loss simulation

Figure 2.3: Transmission loss simulation using the arctic sound speed profile.

As the acoustic ray propagates underwater, it will bend away from regions of higher sound speed. This is due to the refraction of the acoustic ray between different regions of sound speeds. This refraction of the acoustic ray obeys Snell's Law, which states that the ratio of the sine of the incident angle of a sound wave onto a boundary of two different mediums and the sine of the refracting angle is equivalent to the velocities of the sound wave in the two mediums, or the ratio of the index of refraction of the two mediums. From Figure 2.4 Snell's law can be written as,

$$\frac{\sin\theta_r}{\sin\theta_i} = \frac{c_2}{c_1} = \frac{n_1}{n_2}, \tag{2.8}$$

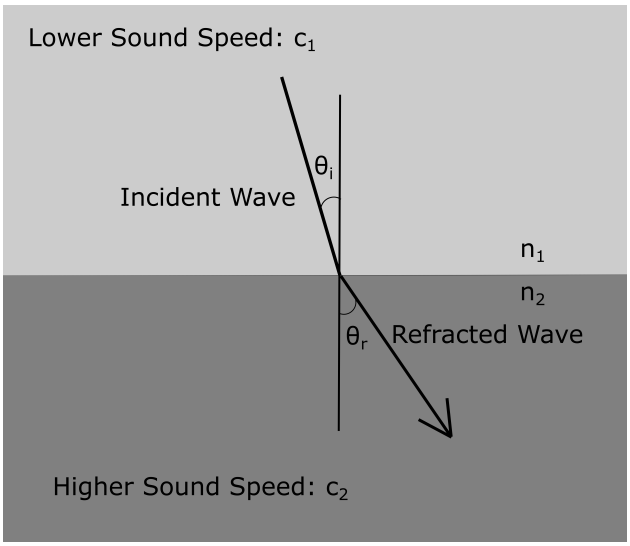

Figure 2.4: Ray refracting between two mediums of different sound speeds.

where, n_1 and n_2 are the refraction indicies of the two mediums, c_1 and c_2 are the speed of sound in the two mediums, θ_i is the incident angle, and θ_r is the refracted angle. Using Equation (2.8), the acoustic ray will bend away from regions of higher sound speed towards regions of lower sound speed.

In Figure 2.3b a transmission loss simulation is shown using the Bellhop ray tracing simulator developed by Porter and Liu [28], which will be described in more detail in Chapter 4. In Figure 2.3b, the rays tend to stay within the duct due to refracting away from regions of higher sound speeds. First, the rays can be seen to bend over the range of 10 km. In particular, this can be observed for those low departing angles that are seen to remain within that duct above 100 meters. Second, there is very little energy in specific regions, particularly below 150 meters at long range. Finally, some of the rays add constructively or destructively at specific points, thus creating a fading effect.

In addition to fading, the acoustic signal is subject to various loss mechanisms from the ocean environment. These losses include, absorption, scattering and reflection losses all of which affect the acoustic signal. At frequencies above 10 kHz, absorption affects the signal by way of the transfer of heat from the acoustic energy into the medium. Below 10 kHz, acoustic energy is lost to chemical processes related to salts dissolved in seawater [31]. In addition the acoustic signal will reflect off the air-water boundary as well as the bottom, which can cause the signal to scatter and potentially not reach the receiver. This is referred to as reflection and scattering losses. Scattering losses may also occur inside the water column, where biological

organisms, suspended sediment particles, bubbles, or physical processes (e.g. mixing) can be present. When the signal reaches the bottom, a portion of the acoustic energy may transfer into the bottom causing additional losses. The bathymetry of the acoustic channel can also cause shadowing which can affect the acoustic signal. Outcrops, large boulders, and other ocean bottom features can block or interfere with the acoustic signal. The signal is blocked and therefore not present immediately downstream of the bottom feature. This is known as shadowing due to bathymetry.

2.1.2 Propagation Delay

Propagation delay is defined as the time it takes for the acoustic signal to propagate from a source, or a transmitter to a point, or a receiver. Assuming the acoustic signal propagates in all directions from the source and the presence of reflective boundaries or scatterers, there will be different signal intensities arriving at the receiver at different times. This is considered to be multipath, where the acoustic signal takes multiple paths to reach the receiver, whether it be a straight line, single or multiple bounces. In this thesis, the focus will be on line-of-sight and single surface bounce propagation delay. As the signal propagates out from the transmitter in all directions, a single ray represents one particular path of the signal. Rays are perpendicular to propagating wave fronts. In the case of a monopole source in a homogeneous medium with no boundaries, the wave fronts are spherical and the ray paths are radial. Drawing a ray from the source to a point in the far-field is considered to be LOS. Drawing a ray that bounces once off the surface is considered a single surface bounce. A simple analytical model using geometry and trigonometry can be used to estimate the propagation delay for a LOS path, and a single surface bounce path. Let's define a flat homogeneous ocean waveguide consisting of a constant SSP, with one transmitter and one receiver placed near the bottom, with the LOS and surface bounce paths, as shown in Figure 2.5.

Assuming the speed of sound in water to be represented as c, and a straight line distance between the transmitter and the receiver represented as d, the time it takes for the LOS signal to reach the receiver is

$$t_{LOS} = \frac{d}{c}. \tag{2.9}$$

A single surface bounce results when the signal leaving the source or transmitter at an

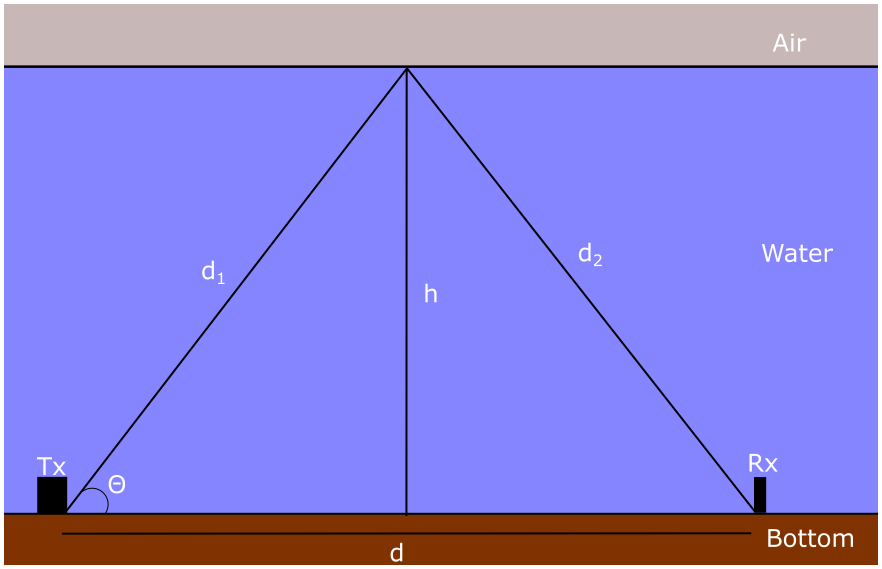

Figure 2.5: Geometrical propagation delay model

angle, reflects off the surface to the receiver. Let d_1 be the distance from the source to the surface, and let d_2 be the distance from the surface to the receiver. Since the sea surface is flat and the transmitter and receiver are at the same depth, $d_1 = d_2$. Both the source and the receiver are at the bottom of the waveguide at a depth of h and at a distance of d apart. Using the constant sound speed, c, the time of arrival for the surface bounce is represented as

$$t_{SB} = \frac{d_1 + d_2}{c}. \tag{2.10}$$

Since the depth of the waveguide, and the distance between the transmitter and the receiver is known, the surface bounce path can be calculated with trigonometry. The launch angle of the ray with respect to the horizontal, θ, can be found geometrically to be $\theta = \arctan\left(\frac{2h}{d}\right)$. This can be used to determine the length of the ray from the source to the surface, d_1 such that

$$d_1 = \sqrt{\left(\frac{d}{2}\right)^2 + h^2} \tag{2.11}$$

The total distance for a single surface bounce is represented as

$$d_1 + d_2 = 2\left(\sqrt{\left(\frac{d}{2}\right)^2 + h^2}\right). \tag{2.12}$$

Substituting Equation (2.12), into Equation (2.10) produces a time of arrival for a single surface bounce. Theoretically, in an environment where the SSP is constant throughout, a single surface bounce will take more time to reach the receiver than a LOS path, $t_{SB} > t_{LOS}$, due to the additional distance travelled. In reality, the SSP is dependent on temperature, pressure, and salinity. Where temperature and salinity often increase near the surface, it is possible that the increasing sound speed as the transmission travels to the surface could result in a shorter overall delay time as compared to the LOS path.

2.1.3 Multipath Arrival

The maximum delay spread is the difference in time between the first and last arrivals of the signal. In addition, there will be path arrival times between the shortest and longest arrival times. As the ambient noise increases, the time spread will reduce as late-arriving, weaker paths are masked. With the presence of high noise, the separation in the multiple paths becomes harder to distinguish. The root mean squared (RMS) delay spread is a standard deviation value of the delay between path arrivals that is proportionally weighted to the amplitude of the arrival signals. The formula for the RMS delay spread is written as

$$\tau_{rms} = \sqrt{\bar{\tau^2} - \bar{\tau}^2}, \tag{2.13}$$

where $\bar{\tau^2}$ is the average squared delay in seconds, $\bar{\tau}^2$ is the mean excess delay in seconds, such that τ_{rms} is the RMS delay spread in seconds. The average squared delay and the mean excess delay are related to the amplitude and the time delay between path arrival signals expressed respectively as

$$\bar{\tau^2} = \frac{\sum a_i^2 \tau_i}{\sum a_i^2}, \tag{2.14}$$

and

$$\bar{\tau}^2 = \frac{\sum a_i^2 \tau_i^2}{\sum a_i^2}, \tag{2.15}$$

where a_i is the amplitude of the path arrival in pascals and τ_i is the time delay between path arrivals in seconds. The RMS delay spread is important as it affects the inter-symbol interference. If the symbol duration is significantly larger than the delay spread, there will not be any inter-symbol interference.

2.1.4 Doppler Spread and Doppler Shift

The Doppler shift is the change in frequency of a wave produced from a moving source to an observer moving relative to the wave source [32]. The Doppler shift depends on the frequency, speed of sound in the medium, the speed of the source, and the speed of the observer. In the Grand Passage environment, large tidal flows can create motion in both the transmitter and receiver, creating a Doppler shift. A Doppler spread is when the acoustic channel has multipath, the receiver at a position will receive one signal, and then receive an additional signal, with a different Doppler shift. The phase shifted multipath signals then add together, and where the delay varies as a function of time, this creates a Doppler spread that is observed as a spreading of the carrier signal in the frequency domain [32].

Let the speed of sound in the water be c in meters per second, and the speed of motion in the transmitter be v and respectively in meters per second [32]. If f_o is the carrier frequency in hertz, and the source and receiver are moving towards each other then the perceived frequency, f' at the receiver is

$$f' = f_o \left(\frac{v}{c}\right). \tag{2.16}$$

To determine the Doppler shift, an averaged Fast Fourier Transform (FFT) technique over a specified number of windows is used on the filtered baseband signal. When there is no mean Doppler shift, the graph of the Doppler spread will have a peak at zero, and the Doppler spread is measured as the frequency at which the spectrum of the signal has attenuated by 3 dB with respect to the peak.

2.1.5 Effect of Surface Waves and Current

The previous sections assumed that the ocean surface was a static and perfect reflecting boundary. In reality, the ocean surface is constantly in motion. Moving air above the water pushes on the air-water surface creating waves, that are typically periodic over short periods of time. This in turn causes losses due to air bubbles near the surface, and scattering of the acoustic signal when it reflects off the air-water boundary.

Surface scattering of the acoustic signal (the pressure field) has been modelled by Thorsos [33]. The scattered pressure field is determined by modelling the time-varying surface

in one dimension, and represented by the Helmholtz integral equation. The Kirchhoff approximation is used to simplify the model by assuming the scattered field is only dependent on the incident field, and not the total field. In addition, Thorsos modelled random surface shapes using white noise filtered with a Gaussian spectrum which is used as an accurate representation of the ocean surface.

Figure 2.6 shows the channel amplitude in decibels at low and high-flow from four 10 second tones recorded by three Autonomous Multichannel Acoustic Recorders (AMAR-A, AMAR-B and AMAR-C) at distances of 77 meters, 567 meters, and 1060 meters respectively. The frequencies of the tones were 8 kHz, 10 kHz, 12.5 kHz and 16 kHz. The blue line represents the channel amplitude during low flow (e.g. high or low tide) conditions, and the orange represents the channel amplitude during high-flow (e.g. mid-tide) conditions. The top plot is the AMAR-A or the 77 meter distance, the middle is AMAR-B or the 567 meter distance, and the bottom plot is AMAR-C or the 1060 meter distance. The time duration is five seconds, half the duration of a single tone. Tones were used to extract fading characteristics of the channel, and a matched filter used to obtain the amplitude as a function of time.

As the wave height varies as a function of time, the reflections off the fluctuating surface affect the small scale propagation delay of the surface reflected signal. The scattering effect depends on the surface wave size in comparison to the acoustic wavelength, and can results in the energy of the signal redirected in random directions[31]. This results in a major change in pressure loss at the receiver. This will occur over very short time scales for the duration of one pulse. This can be seen in Figure 2.6 as where the channel amplitude within a single five second tone drops to a large negative decibel value.

This is considered to be fading where the signal interacts with other signals that degrade the strength of the original signal. Fading is typically caused by the original signal combining with other multipath signals or noise. Figure 2.6 also shows that significantly more fading occurs at high-flow. In addition, as the signal reflects off different parts of the wave, this tiny displacement will create an arrival time variance with multiple transmissions. If there are n number of signal transmissions, the variance of the surface bounce propagation delay can be calculated using

$$S_{SB}^2 = \frac{\sum(t_{SB_i} - \overline{t_{SB}})^2}{n-1}, \tag{2.17}$$

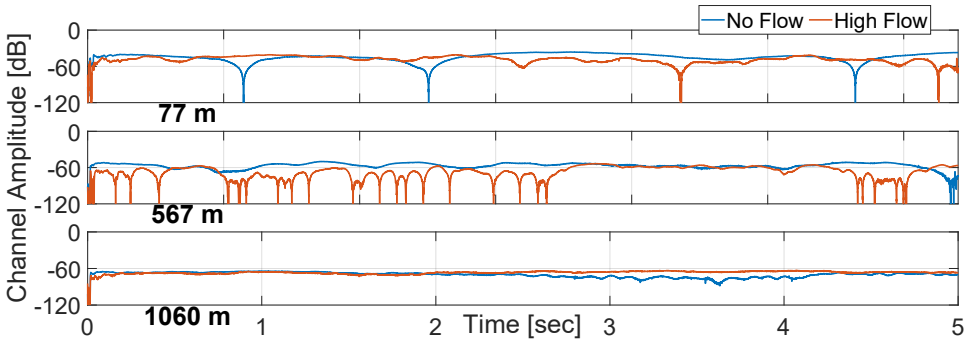

(a) 8 kHz Tone

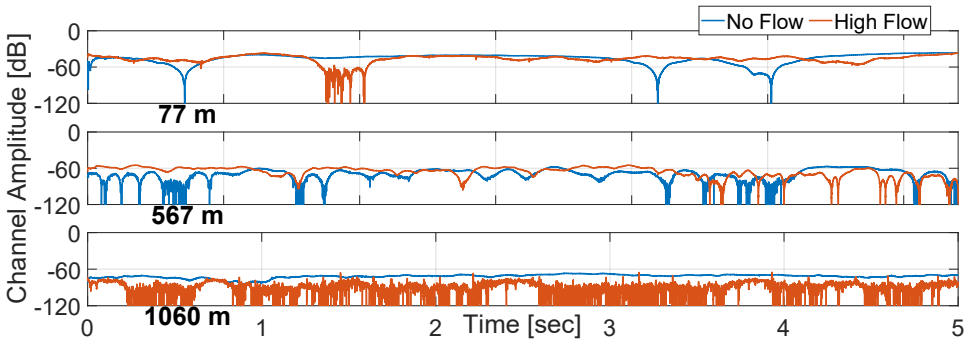

(b) 10 kHz Tone

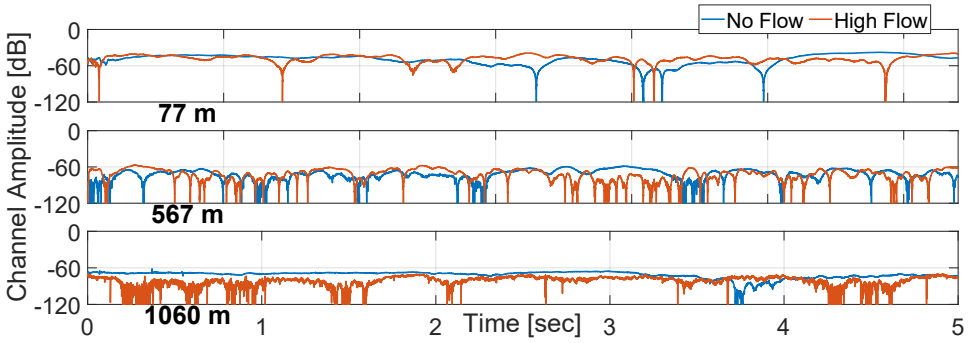

(c) 12.5 kHz Tone

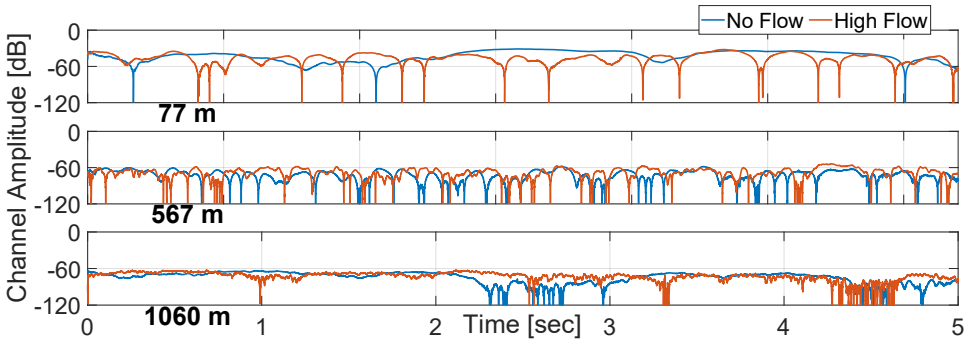

(d) 16 kHz Tone

Figure 2.6: Channel amplitude from four tones at 8 kHz, 10 kHz, 12.5 kHz, and 16 kHz over a five second duration.

where t_{SB_i} is the i^{th} surface bounce arrival time, and $\overline{t_{SB}}$ the mean value of all surface bounce arrival times.

Mean flow and turbulence are different forms of water movement. The mean flow is an average value of the water flow in a steady direction over a time period. Turbulence is defined as random changes in water flow and direction not captured by the mean. Turbulence is an energetic, rotational and eddying state of water motion [34]. Areas of turbulence can be advected within the flow. In tidal environments, the mean and turbulent flows may have an impact on the signal propagating through them.

The propagation channel between the source and the three receivers is approximately parallel to the direction of mean flow in the area. Let's define a nominal sound propagation velocity c_{nom} that is approximately constant as a function of depth and range, a flow speed that represents the mean flow, $\overline{c_f}$ parallel to the propagation channel and a turbulent flow component c'_f that is range and depth dependent. Both $\overline{c_f}$ and c'_f vary as a function of time on a tidal scale, but can be considered constant during a single acoustic transmission window. The travel time t_{LOS} for the LOS between the transmitter and the receiver situated at the same distance d from the receiver is defined as

$$t_{LOS} = \frac{d}{c_{nom} + \overline{c_f} + \int_0^{s_d} c'_f(s)ds}. \tag{2.18}$$

The surface bounce (SB) travel time is now defined as

$$t_{SB} = \frac{d_1 + d_2}{c_{nom} + \overline{c_f} + \int_0^{s_d} c'_f(s)ds}, \tag{2.19}$$

where $s = s(r, z)$ along the LOS and surface bounce ray, d_1 defined in (2.11) is the distance to the surface, and $d_2 = d_1$ as the distance from the surface to the receiver. The turbulent flow induces a variability in the time of arrival for each transmission between the transmitter and receiver. The impact of this phenomena will be studied in Chapter 4, Section 4.2. It will be demonstrated in simulation and confirmed using measurements where the turbulent flow induces significant transmission loss variations as well as delay spread variations on the propagation channel.

2.1.6 Ambient Noise

Ambient noise is the combination of all the undesirable sounds within the environment. These sounds or noises are created from various ocean factors such as pressure changes,

ocean waves, bubbles, wind, rain, ocean turbulence, thermal agitation, marine animals, human-made noise, breaking ice, and biological noise. The ambient noise is a part of the total noise background that is detected by omnidirectional hydrophones. The total noise includes the ambient noise along with electrical noise generated within the hydrophone itself, and the flow noise created on the surface of the hydrophone [35]. In shallow water environments, the ambient noise is dominated by three major components: shipping and industrial noises, wind and wave noise and biological noise [36]. In addition to the three dominant ambient noise sources typical of a shallow environment, noise will also be generated from turbulence. Figure 2.7 shows the received noise spectrum level in $dB\ re\ 1\ \mu Pa$ at two time periods with contrasting high and low flow speeds. It is evident that there is an increase in the received spectrum level of noise associated with the high-flows. The high-flow also shows a few increases in the spectrum level between 100 and 1000 Hz, which could be noise from the ferry. At higher frequencies, between 1-10 kHz both curves seems to increase, which could be high frequency noise from surface agitation and bubbles.

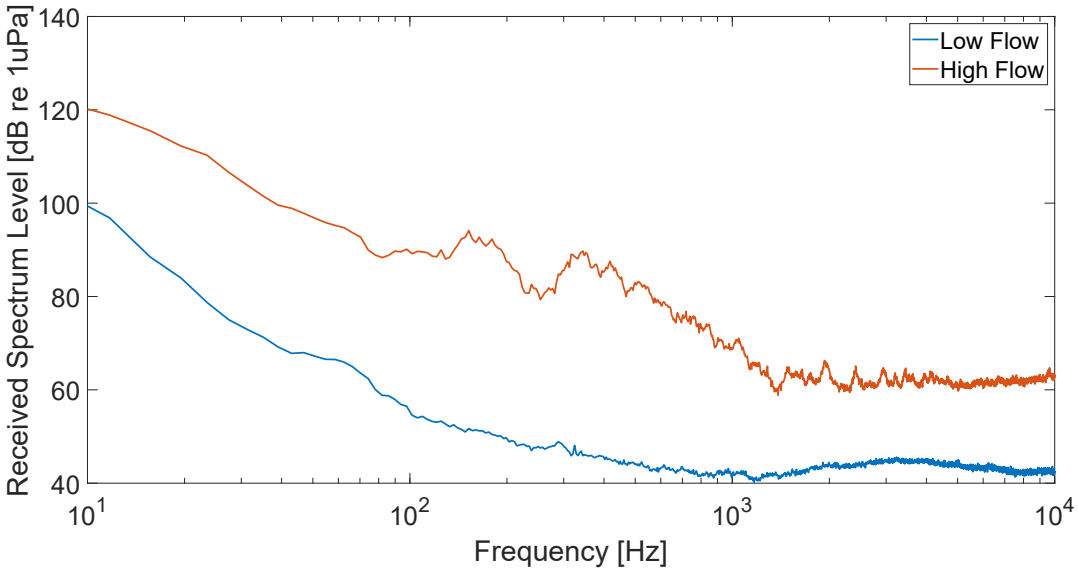

Figure 2.7: Noise spectrum level versus frequency in grand passage.

2.2 Grand Passage Experiment

An acoustic transmission experiment was carried out in Grand Passage, located in the Bay of Fundy between Briar Island and Long Island Nova Scotia, Canada. The experiment was conducted between September 21st to October 26th, 2018 covering 35 days. The work was funded by the Ocean Energy Research Association (OERA). It was planned and carried out by JASCO Applied Sciences, in collaboration with Prof. David Barclay of the Dalhousie Oceanography Department. Luna Sea Solutions provided community engagement, field support and flow modelling. Dalhousie Oceanography also provided the moorings, labour, and the acoustic Doppler current profiler (ADCP).

Figure 2.8 shows a map of the deployment area in Grand Passage, with a Universal Transverse Mercator (UTM) coordinate system. The bathymetry between the transmitter and the three receivers is primarily flat with a maximum depth of around 24 meters, and a minimum of approximately 14 m.

An acoustic projector was placed on the bottom of Grand Passage at a depth of 23 meters. Its location is noted as SS on Figure 2.8. Every thirty minutes, the sound projector emits a sequence of known signatures, which are received by three, four-element sensor arrays positioned at various distances from the transmitter. The transducer source level (SL) is 180 dB re 1 μPa/1 m, and at the receiver the hydrophone sensitivity is -204 dB re 1V/μPa.

Each of the three sensor arrays are comprised of four omni-directional hydrophones mounted on JASCO Applied Sciences' Autonomous Multichannel Acoustic Recorders (AMARs). The arrays were placed at three distances denoted as AMAR-A, AMAR-B, and AMAR-C shown in Figure 2.8. The distances from the acoustic projector are 77, 567, and 1060 meters respectively. Each of the hydrophones have a bandwidth of 125 kHz, and the output is sampled at a rate of 64 kHz. The sensitivity of the hydrophones is quoted to be -204 dB re 1V/µPa.

The bottom composition in Grand Passage consists of only gravel and sand, and beyond a distance of 700 meters between the transmitter and receiver, glacial till [2]. The two bottom compositions are along the propagation path. The bathymetry of Grand Passage between the transmitter and receivers is shown in Figure 2.9.

It should be noted that every 30 minutes, a ferry transports passenger cars between Briar and Long Islands. The ferry's propeller and machinery produce significant acoustic noise in the channel. There is also a large population of marine animals in the area, including but

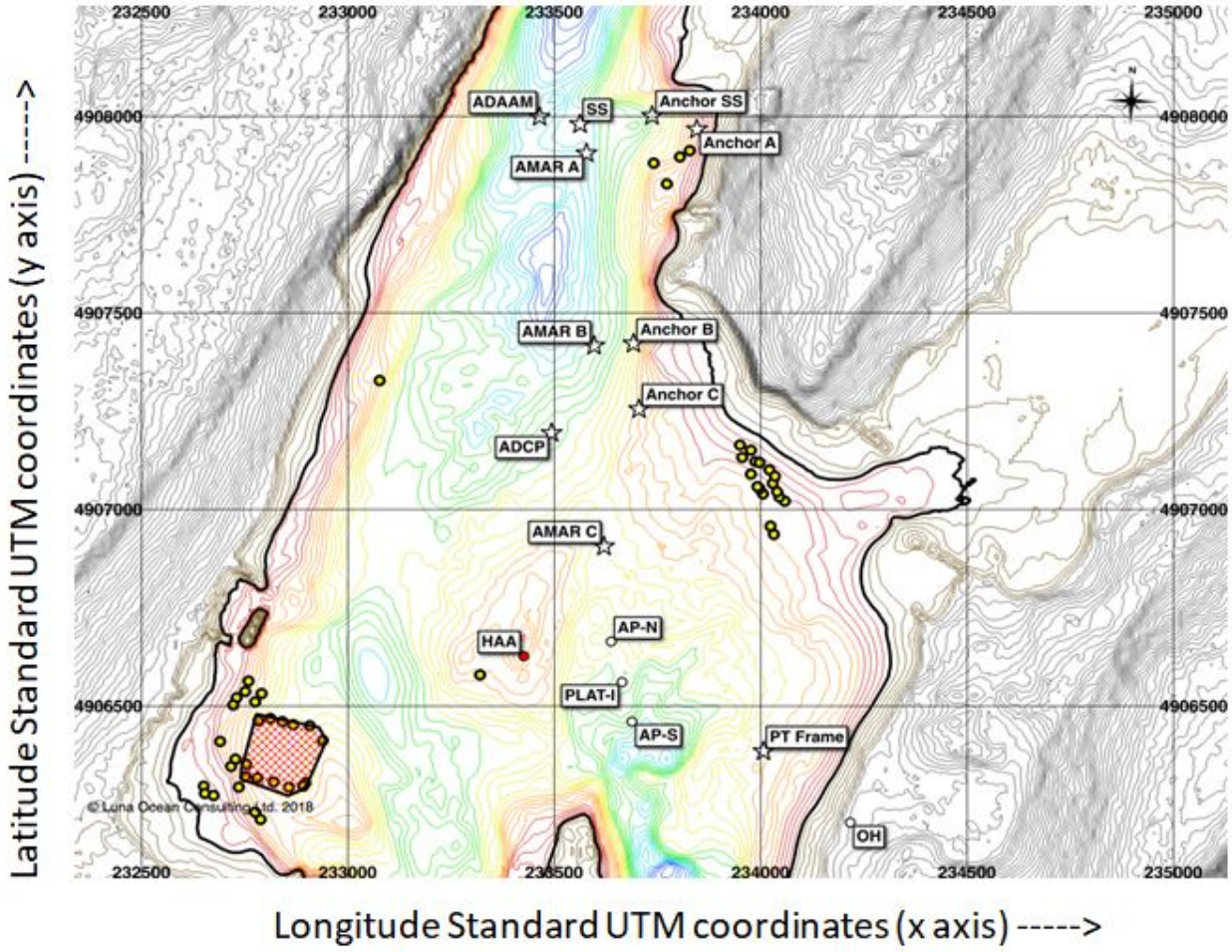

Figure 2.8: Map of Grand Passage with Universal Transverse Mercator (UTM) coordinates. The equipment includes an Acoustic Doppler Current Proflier (ADCP) by Dalhousie University [37]; Autonomous Multichannel Acoustic Recorders (AMARs) [38]; PLAT-I: Blackrock Tidal's community scale tidal turbine platform with AP-N and AP-S north and south anchor points for PLAT-I; Acoustic Doppler Aquatic Animal Monitoring system (ADAAM); HAA navigation buoy; PT-Frame a bottom mounted temperature and pressure sensor.

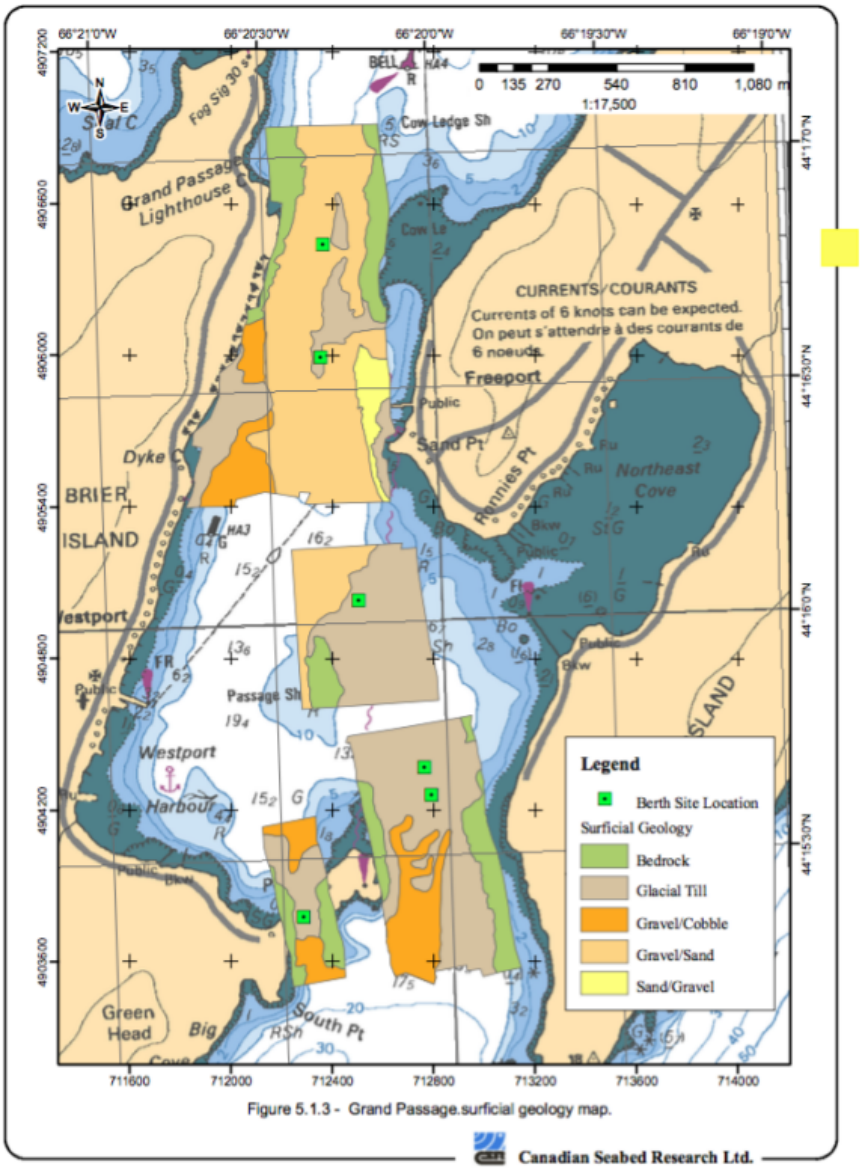

Figure 2.9: Grand Passage bathymetry showing latitude, longitude and the depth in meters from the Canadian Seabed Research Ltd. [2]

not limited to harbour porpoises, and whales. Since an acoustic source was deployed for the duration of the trials, a marine assessment was conducted prior to the start of the trials to ensure that no harm would come to the animals.

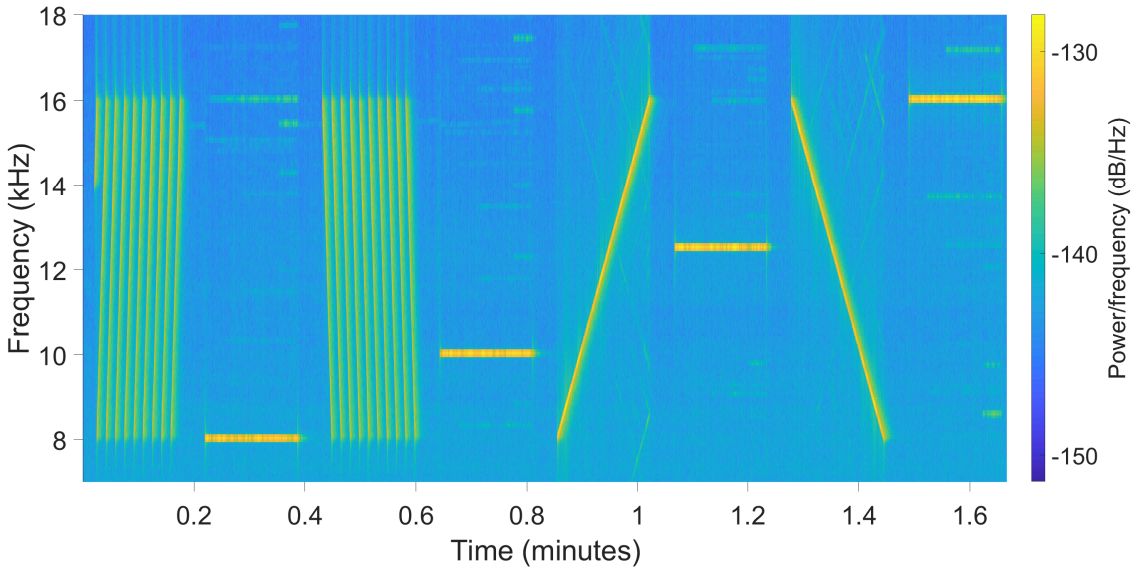

Figure 2.10: Frequency spectrum of the transmitted signal.

The transmitted acoustic signature consisted of 10, one-second linear frequency modulation (LFM) up sweeps, 10 one second LFM down sweeps, four 10 second tones centered at 8 kHz, 10 kHz, 12.5 kHz, and 16 kHz, and two 10 second LFMs: one up sweep, and one down sweep. Each LFM had a bandwidth with a starting frequency at 8 kHz. This sequence of signals was received every thirty minutes, from September 21st, 2018 to October 26th, 2018. The spectrogram of the transmitted signal as a function of time is shown in Figure 2.10. The signal multipath can be seen on each transmission, visible as a decaying tail after the most powerful direct arrival. Vertical lines of higher intensity at the beginning and end of each transmission as the transducer is switched on and off is shown. Also some harmonics and overtones due to distortion present.

The data was recorded continuously over the 35 days, and a procedure to extract the received information from the individual sound files was applied, to produce a compressed database with the useful data from all sensor arrays. It should be noted that the transmitter and receiver clocks were not synchronized, requiring compensation for clock drift.

2.2.1 Measured Flow

The flow speed and direction was collected over 14 days, at a sampling period of five minutes using an Acoustic Doppler Current Profiler (denoted as ADCP in Figure 2.8) from September 22nd, to October 5th. The ADCP recorded depth profile of flow, along the North, East, and vertical axes. Using the ADCP pressure measurement, the tide height was also recorded. Given the tide height, the primary tidal period in the area was calculated to be around 12.3 hours. Figure 2.11 shows the measured flow speed along the acoustic channel axis as well as the tide cycle over 48 hours, where for each time sample, a histogram of flow velocity is produced. Each bin in the histogram represents a one half hour time period, and the number of observations in each bin represents the velocity density for that time period. As the flow speed increases, so does its variance, during both the flood tide corresponding to a rising water level, and ebb tide corresponding to a falling water level. Flow speeds as high as 2.5 meters per second were recorded.

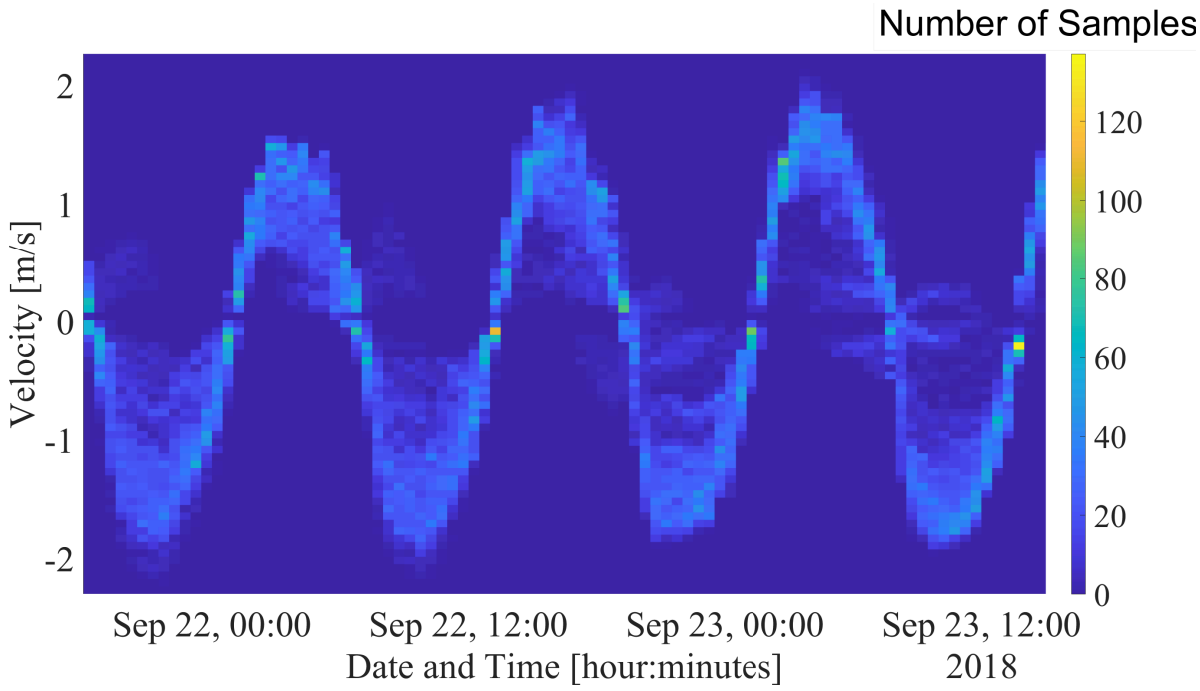

Figure 2.11: Histogram of the flow as a function of time for a duration of 48 hours. Bright yellow represents a region of high density.

Figure 2.12 shows the depth averaged flow speed, computed from the 69 depth bins measured by the ADCP, over a period of three days. West was established as a reference

direction, at zero degrees for the depth averaged flow direction shown in Fig 2.12b. The water depth was used to capture the tides.

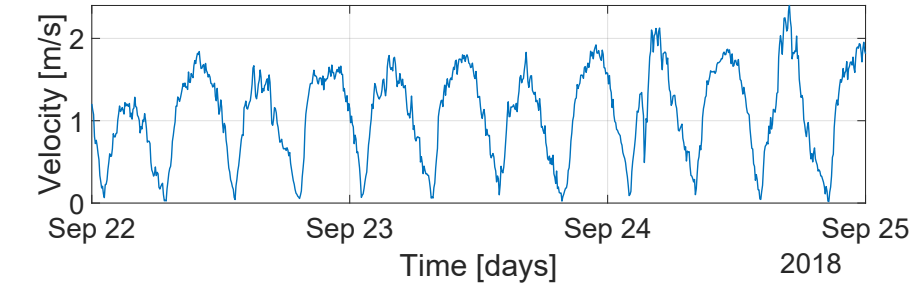

(a) Flow Magnitude

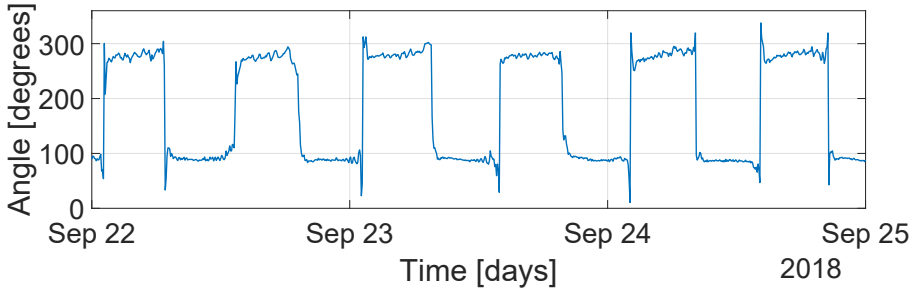

(b) Flow Direction (West is 0 degrees)

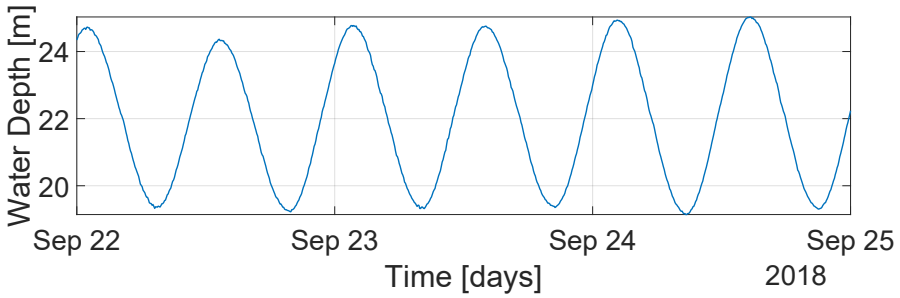

(c) Tide Height

Figure 2.12: Data showing the magnitude of the flow, angle of the flow, and the tides over three days

From Figure 2.12b, the flow of water changes direction by 180 degrees from the flood and ebb tides. At the exact time of high and low tides seen in Figure 2.12c, the flow speed decreases to zero, as shown in Figure 2.12a.

2.3 Chapter 2 Summary

In this chapter, first, of the physics of propagation was discussed, including delay spread, transmission loss, arrival time and the effect of flow and surface waves.

The chapter provided, an overview of the physical environment at Grand Passage, in the Digby neck of Nova Scotia, Canada. A 35-day experiment was described where tones, and LFM signals were transmitted to three recorders each equipped with four hydrophones. The three recorders were placed at three different distances from the acoustic source. In addition, an ADCP was placed to record pressure data, and flow speeds.

In regions where tides have a significant impact on flow, the acoustic channel is typically shallow. For the described deployment conditions the nominal channel depth is 24 meters, and the ADCP measured flow speeds slightly greater than 2.5 meters per second. The impact of flow speed on the propagation characteristics will be demonstrated.

Chapter 3

Data Processing and Analysis

This chapter will discuss the data processing conducted on the measured data. The database of the acoustic recordings during the experiment conducted in Grand Passage from September 21st to October 26th was provided by JASCO Applied Sciences.

The data processing described in this chapter serves to extract the channel characteristics, including the channel gain, delay spread, Doppler spread, and propagation delay. The LFM signals will be processed to obtain the time of arrival, channel gain, and delay spread. The tones will be processed to obtain the Doppler spread.

The rest of this chapter is organized as follows; in Section 3.1, the acoustic database from the hydrophone loggers over 35 days is analyzed to determine the channel characteristics; in Section 3.2, the 14 day ADCP measured flow velocity and tide height is extrapolated over the 35 day experiment period and a relationship between the tide and flow speed is presented, in Section 3.3, the chapter contributions are summarized.

3.1 Characterization of the Acoustic Channel

In this section, the recorded data was analyzed to characterize the statistical properties of the acoustic channel. Specifically; in Section 3.1.1, the procedure to obtain the channel impulse responses every 30 minutes will be described; in Section 3.1.2, an analysis of the channel gain will be described; in Section 3.1.3, the delay spread will be analyzed; in Section 3.1.4, the time of arrival will be analyzed; finally, in Section 3.1.5, the Doppler spread will be assessed.

3.1.1 Acquisition of Channel Impulse Response Sequence

To obtain the channel impulse response (CIR), signal processing must be applied to the recorded data. The fundamental signal processing steps are summarized in Figure 3.1. Recall that, as mentioned in Section 2.2, the first sequence consists of 10 one-second consecutive up signals, and 10 one-second consecutive down signals. It should also be noted that there was an issue in the definition of the transmit signal and the first one-second LFM up signal was

not fully recorded; as such, it was neglected in this analysis. Rather than strictly averaging the nine up signals or the 10 down signals both the nine up and 10 down LFM signals were analyzed to obtain a more accurate statistical analysis which will be discussed in Chapter 5.

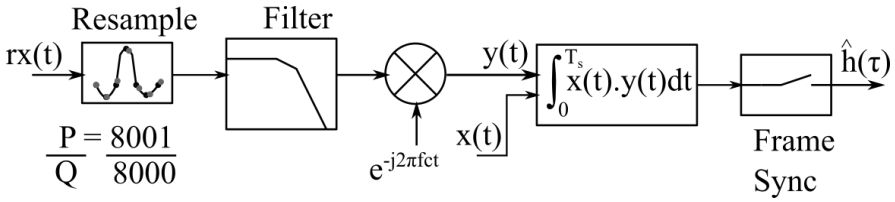

Figure 3.1: Signal processing steps applied on the recorded data to obtain the sequence of CIRs

The first step in the signal processing is to resample the recorded data, denoted as $r(t)$. Within the nine one-second LFM up or 10 LFM down signals, there is a small drift in time delay between each individual LFM signal over the nine or 10 seconds. This is due to the hardware sampling rate being slightly higher or lower than the nominal value of $F_s = 64000$ samples per second, which transfers from the hardware into the database. One solution to address this is to use the `resample` function provided by MATLAB. This function up samples the input signal by a factor P, passes it through a band limiting filter, and decimates it by a factor Q. This P/Q factor is the greatest common denominator between the nominal sampling rate and the hardware's sampling rate. The factor becomes a multiplicative factor to correct the hardware's sampling rate to the nominal sampling rate. In this work, each window is applied the same resampling factor equal to $P/Q = 8001/8000$. This time delay drift occurs when the transmitter is in motion, and not fixed in space, and can create a channel impulse response with a slope that changes in time. In this case, however, the transmitter was fixed to the bottom, with limited motion.

After resampling the data, a filtering process is used to filter out any noise or unwanted frequencies. The filter used was a band-pass filter that had a lower cutoff frequency of 7.9 kHz, and an higher cutoff frequency of 16.1 kHz. The band-pass filter was chosen since the data is still modulated onto the carrier wave.

Following the filtering process, the next step is to demodulate the signal. At the transmitter, the data is modulated onto a carrier wave with a frequency of $f_c = 12\ kHz$, which is the middle frequency in a LFM signal. The carrier signal with the modulated data propagates through the environment in what is considered the pass-band signal. Therefore, at the receiver the data needs to be demodulated from the pass-band down to base-band, where

the carrier signal is discarded, and the data remains. This consists of a multiplication of the pass-band signal with a shifted carrier signal as $e^{-j2\pi f_c t}$. Next an estimation of the channel will be determined.

After resampling the signal, filtering and demodulating, the estimation of the channel will be determined from a cross-correlation and a frame synchronization. The cross-correlation looks at the similarity of two signals that are used. In this case, the two signals are the LFM up signal and LFM down signal in the file. A reference LFM signal, denoted as $x(t)$, is used in the cross-correlation with the processed signal, $y(t)$. The increasing and decreasing reference LFM signals are expressed at base-band in complex notation to be

$$x(t)_{up} = e^{j2\pi\left(\frac{B}{Ts}t^2 + f_o t\right)}, \tag{3.1}$$

$$x(t)_{down} = e^{-j2\pi\left(\frac{B}{Ts}t^2 + f_o t\right)}, \tag{3.2}$$

where B is the signal bandwidth in hertz, T_s is the symbol time in seconds, f_o is the fundamental frequency in hertz, and t is the signal time also in seconds [39]. At base-band, $f_o = 0$. For this application, the signal bandwidth is between 8 kHz, and 16 kHz, its period is $T_s = 1$ *second*, the fundamental frequency is 8 kHz. With the two expressions for the LFM up signals and LFM down signals, the signal $y(t)$ is then cross-correlated with the reference signal $x(t)$ to determine an estimate of the channel impulse response $\hat{h}(\tau)$, expressed as

$$R_{xy}(\tau) = \hat{h}(\tau) = x(t) \star y(t) = \int_0^{T_s} \overline{x(t-\tau)} y(t) dt. \tag{3.3}$$

In Equation (3.3), $\overline{x(t)}$ is the complex conjugate of the reference signal, $y(t)$ is the filtered received signal, t is the signal time in seconds, τ is the delay in seconds, and $R_{xy}(\tau)$ represents the cross-correlation between $x(t)$ and $y(t)$.

Note that the accuracy of the estimate of the channel $\hat{h}(\tau)$ depends on the characteristics of the signature, specifically on its auto-correlation function. Ideally, the signature auto-correlation function is unity at zero-lag, and zero elsewhere. In reality, the auto-correlation of the LFM signal is shown in Figure 3.2. As can be observed, the main lobe has a width of 0.25 msec which limits the temporal resolution channel impulse response. In addition, the maximum sidelobe amplitude is at -13.46 dB with respect to the main amplitude, which raises the noise floor. In practice, any channel path amplitude with a peak above -13.46 above the main peak will be discarded.

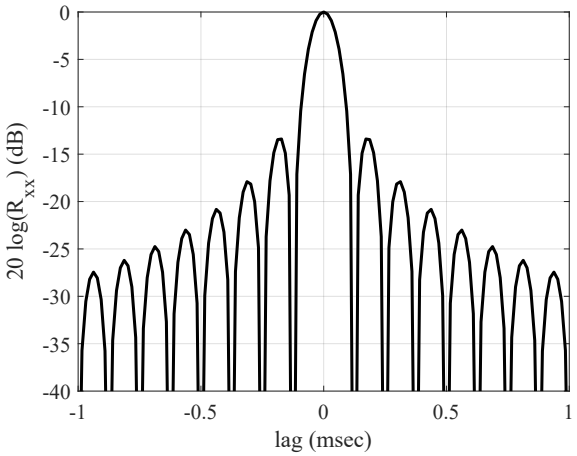

Figure 3.2: Auto-correlation of the transmit signature

With the channel estimation, $\hat{h}(\tau)$, a frame synchronization of the signal is required to address the clock drift. In this experiment, AMAR's clock time periods are not synchronized; therefore, there is a clock drift between the transmitter and the receiver. The clock drift between the transmitter and the receiver can be resolved by synchronizing to the signal on every file in the database. The clock drift can be seen as a small separation in time between each acoustic file. Over all the files spanning 35 days, the accumulated separation in time between the first file and the last file is approximately seven seconds as seen in Figures 3.3a and 3.3b. Over 35 days, this works out to a clock accuracy of around 2.5 parts per million, which is considered very good for an autonomous system. Typical micro-controllers can have up to 100 parts per million clock accuracy. However, this clock drift still adds a small offset in the channel impulse response time delays between each 30-minute window.

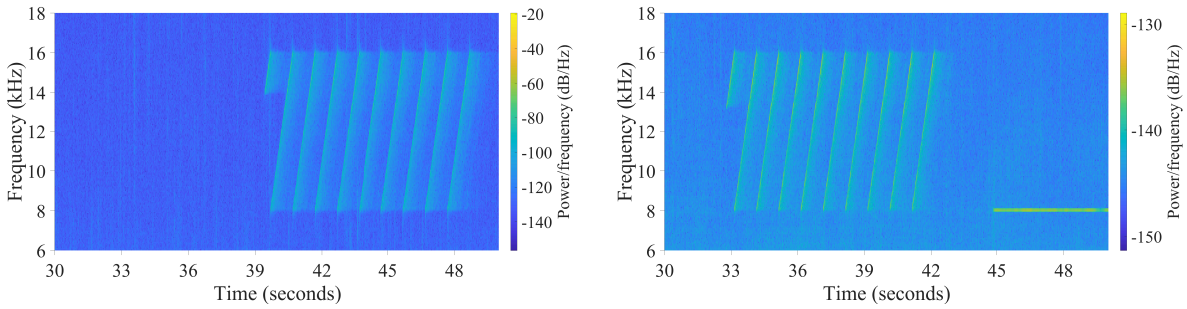

(a) September 21, 2018

(b) October 26, 2018

Figure 3.3: Spectrogram of the 10 LFM up signals showing the clock drift over 35 days from the receiver at AMAR-A

Synchronizing to each 30-minute window aligns the window of received LFM signals to the reference. First the start and end times of the one second LFM up and down signals within each file required synchronization. To synchronize to the beginning of each LFM sequence, the output of the cross-correlation is used to obtain start and end times in each file. Since each LFM signal is one second, a window of one second separates each of the received 9 up signals, and each of the 10 down signals for 19 channel estimations. As shown in Figure 3.4, each of the individual received signals are then individually cross-correlated by aligning the beginning of each received signal, with the signature, and using (3.3). The process is repeated for the up signals and the down signals, and 19 unique channel estimations are produced. Each channel estimation is unique due to the fast changing environment. The first LFM signal at the receiver travelled through a slightly different environment than the next received LFM signal, which may have added other environmental effects, such as increased noise.

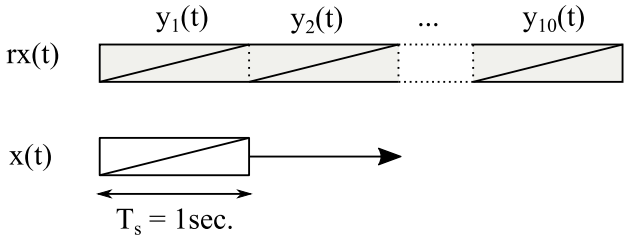

Figure 3.4: Conceptual representation of the cross-correlation with the 10 up signals

3.1.2 Channel Gain

In this section, the channel gain analysis is discussed based on the data obtained from each of the receiver array elements. In an electrical system, the gain is typically a ratio of the output power to the input power. In underwater acoustics, the gain is also expressed with the same relationship; however, the received power is typically significantly smaller than the transmit power due to the signal loss as it propagates through the environment, also known as the channel. If the power at the transmitter is P_{Tx} in watts and the received power is P_{rx} in watts, then the channel gain CG is

$$CG = \frac{P_{Rx}}{P_{Tx}}. \tag{3.4}$$

From the hardware perspective, the digital signal at the transmitter is converted to

an analog signal with a digital-to-analog converter. The analog signal is then modulated, amplified and converted into an acoustic pressure wave at the transmitter with a piezoelectric material that converts the analog signal into pressure waves. The acoustic signal travels through the underwater environment and is received at the hydrophone as a series of pressure waves. The hydrophone also consists of a piezoelectric material that converts the pressure waves into a voltage. The hydrophones used in the Grand Passage experiment had a sensitivity of $S = -204$ dB re 1V/μPa; however, at the frequency range of 8 kHz to 16 kHz, they were calibrated to a sensitivity of $S = -164$ dB re 1V/μPa. The analog signal is converted to a digital signal with an analog-to digital-converter. Therefore to convert the digital signal V_{dig} to acoustic pressure, we use and the sensitivity of the hydrophone compared to the full scale of the digital signal is $S_d = -165$ dB re Full Scale/μPa.

$$p_{rx}\ [\mu\text{Pa}] = V_{dig} \cdot 10^{164/20}. \tag{3.5}$$

Alternatively, we can represent the acoustic pressure in decibels using

$$p_{rx}\ [\text{dBm}] = 20\log_{10}(V_{dig}) + 164. \tag{3.6}$$

In practice, in a frequency selective environment, the channel gain is calculated from the channel impulse response, which is determined by comparing the transmitted signal with the received signal. Using the channel impulse response found in Section 3.1.1, the channel gain is then calculated by integrating over the square of the channel impulse response magnitude, $|h(\tau)|^2$. This is applied to the three receivers, AMAR-A, AMAR-B, and AMAR-C.

To obtain the channel gain, information from the source level of the transmitter, the channel impulse response and the receiver sensitivity is required. The transmission loss assuming spherical spreading is between -35 dB to -40 dB for AMAR-A, -50 dB to -60 dB for AMAR-B, and around -60 dB for AMAR-C. The M18C-6.0 projector with an M304 amplifier is provided by Geospectrum. As documented by the manufacturer, it has a source level of 176 dB re μPa @ 1m at 8 kHz, rising to 186 dB re μPa @ 1m at slightly over 10 kHz before decreasing. Therefore, an average transmitter power was chosen to be 180 $dB\ re\ uPa$ @ $1m$ for the channel analysis. Using a transmit source level (SL) of SL = 180 dB re 1 μPa, and a receiver with a sensitivity of $S = -164$ dB re 1 Volt @ 1 μ Pa, the channel gain in units of

dB can be expressed as

$$\mathrm{CG} = \mathrm{SL} - 20\log_{10}\left(\int_0^{\tau_{max}} h(\tau)d\tau\right) + S. \tag{3.7}$$

This analysis was used on the acoustic signal shown in Chapter 2, Figure 2.10 to produce the channel gain plots shown in Figures 3.5a, 3.5b, and 3.5c. Figure 3.5a represents the channel gain at AMAR-A, Figure 3.5b represents the channel gain at AMAR-B, and Figure 3.5c shows the channel gain AMAR-C. The time span used for the analysis is 35 days; however, five days are presented in the figures.

Reviewing Figures 3.5a through 3.5c, one observation is that the one second LFM up and down signals are in the range of -30 to -40 dB at AMAR-A, -60 to -50 dB at AMAR-B, and approximately -60 dB at AMAR-C. This is close to the theoretical transmission loss values. In addition, environmental effects causing a low signal to noise ratio will still produce error in the results. A summary of the average channel gain, variance and an expected theoretical value for each distance for 10 channels are listed in Table 3.1.

Table 3.1: Mean channel gain.

Channel	AMAR-A	AMAR-B	AMAR-C
One	-35.70 ±4.3 dB	-55.63 ±6.1 dB	-65.15 ±2.9 dB
Two	-37.97 ±3.8 dB	-56.92 ±5.9 dB	-67.00 ±2.3 dB
Three	-32.45 ±3.7 dB	-53.95 ±5.2 dB	-
Four	-32.72 ±3.9 dB	-52.56 ±5.3 dB	-
E[CG]	-34.71 ±2.6 dB	-54.76 ±1.9 dB	-66.08±1.3 dB

In addition, there are a few notable outliers in the channel gain, for example where the channel gain is below 20 dB from the nominal value. It is possible that the multipath combined destructively in those conditions, causing deep fades. It can also be qualitatively observed that for the longer two distances, a periodicity can be observed in the data, and this can be attributed to the impact of the tide level on the channel gain. This behaviour is not as apparent for AMAR-A. A further analysis of the effect of tides will be provided in Chapter 5.

3.1.3 Delay Spread

In this section, the delay spread is obtained using the channel impulse response for all receiver elements. As explained in section 3.1.1 above, the signal is resampled to address the small

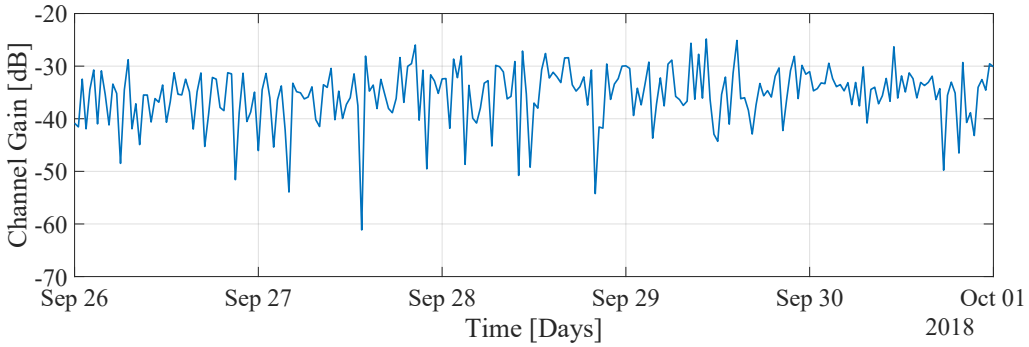

(a) AMAR-A

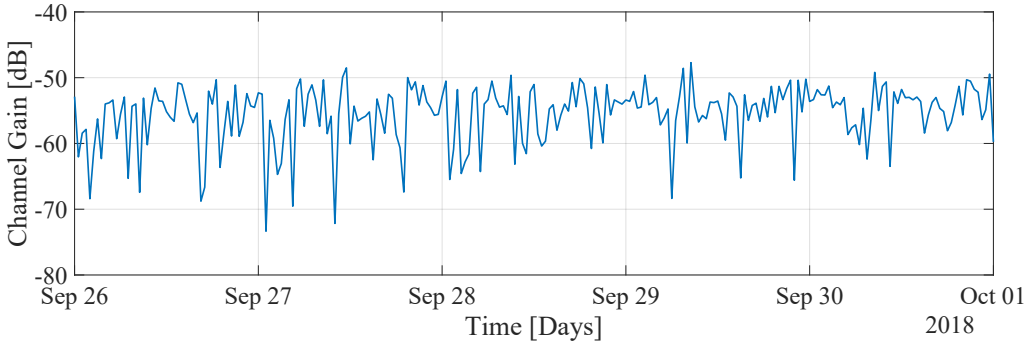

(b) AMAR-B

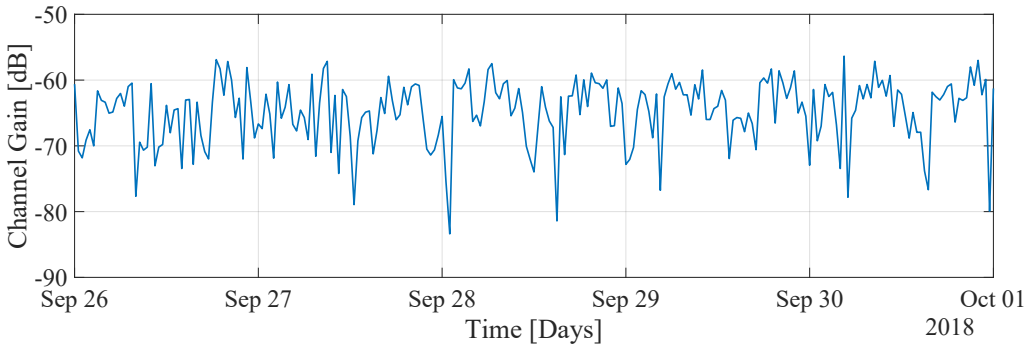

(c) AMAR-C

Figure 3.5: Channel gain over five days.

scale drift within each LFM signal, passed through a band-pass filter, and down converted from a pass-band signal to a base-band signal. The filtered signal is cross-correlated with a reference signal from Equations (3.1) and (3.2) to estimate the channel impulse response using Equation (3.3). With the sampling rate of $F_s = 64000$ samples per second, the cross-correlation output of a single one second LFM signal produces 128000 lags, or discrete-time delays, τ. The majority of the cross-correlation output is below the noise floor; however, a selected window of delays shows the channel impulse response, consisting of the amplitudes $a(\tau)$, and the delays, τ from the various path arrivals. The delay spread, using equations from Chapter 2, is calculated using (2.1.3), discussed in from the averaged squared delay and the mean excess delay, with (2.14) and (2.15), using the amplitudes and delays from the selected window consisting of the channel impulse response from the output of the cross-correlation. The delays and amplitudes are obtained from the channel impulse responses computed for each LFM signal.

The RMS delay spread results can be seen in Figures 3.6a, 3.6b, and 3.6c. Note that it is calculated from the combination of the up signals and down signals. The delay spread in Figure 3.6a appears to fluctuate between 17 ms and 19 ms, in Figure 3.6b it varies between 17 ms and 20 ms, and in Figure 3.6c it varies between 15 ms, and 16 ms. The graph also shows the signal that seems to fluctuates which a characteristic periodicity. This is due to the daily tidal cycle. Large outliers are observed for the delay spread, particularly for 3.6b, and 3.6c, and this can be due to the fact that the channel amplitude experiences deep fades, and in those conditions, the noise at the output of channel estimator may be actually wrongly considered to be channel tap arrivals. The average delay spread, and variance from each figure can be seen in Tables 3.2.

Table 3.2: Mean delay spread.

Channel	AMAR-A	AMAR-B	AMAR-C
One	19.05 ±2.0 msec	18.44 ±2.0 msec	15.50 ±6.0 msec
Two	18.47 ±2.3 msec	20.21 ±2.2 msec	16.35 ±4.8 msec
Three	17.04 ±2.5 msec	17.70 ±3.1 msec	-
Four	18.50 ±3.0 msec	18.74 ±3.9 msec	-
$E[\tau_{RMS}]$	18.26 ±0.8 msec	18.77 ±1.0 msec	15.92 ± 0.6 msec

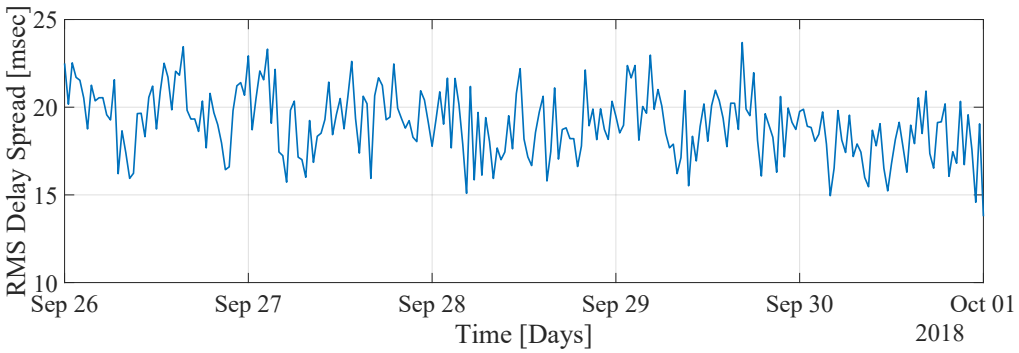

(a) AMAR-A

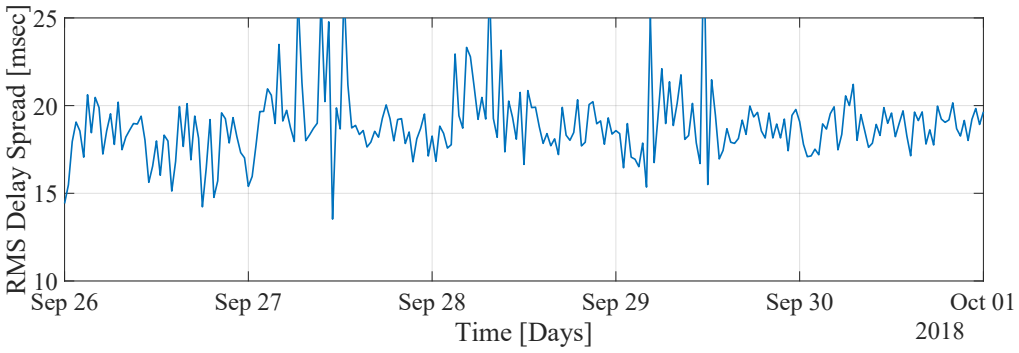

(b) AMAR-B

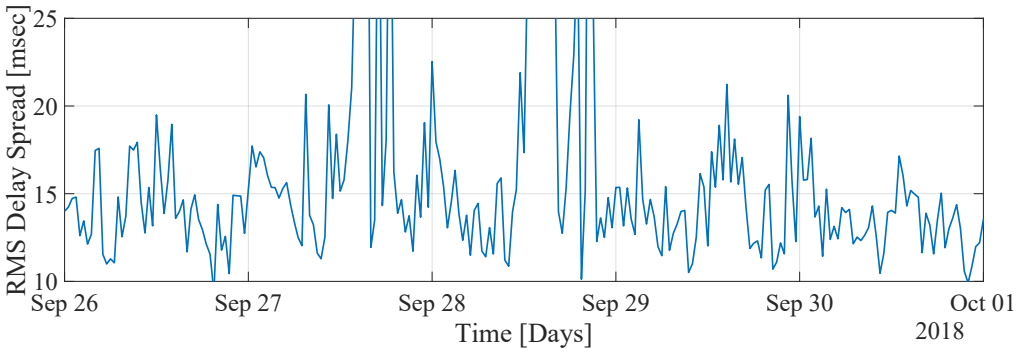

(c) AMAR-C

Figure 3.6: RMS delay spread over five days.

3.1.4 Propagation Delay

In this section the propagation delays from two paths, the LOS path and a single surface bounce path will be discussed. The objective is to determine the mean and variance of the propagation delay observations measured every 30 minutes to assess the impact of flow on the channel characteristics.

At each 30 minute time interval, the mean and variance of the propagation delays are calculated from the 19 samples using (2.17). Since the channel impulse response has multipath, the time of arrival for the LOS and for the first surface bounce are extracted. The LOS propagation delay and the surface bounce propagation delay are represented as two peaks with different amplitudes in the channel impulse response $h(\tau)$. The geometric propagation delay model discussed in Chapter 2 was used to determine a theoretical time separation between the LOS pressure amplitude and the surface bounce pressure amplitude in the channel impulse response. This time delay was calculated to be 9.4 msec. Two peaks in the channel impulse response with this time separation were determined to be the LOS peak and the surface bounce peak. The first peak was considered to be the LOS propagation delay time, and the second peak was the surface bounce propagation delay time. The sampling rate was used with the theoretical time separation of 9.4 msec in the channel impulse response to separate the LOS peak and the surface bounce peak which was determined to be 600 points (64000 points per second multiplied by 9.4 msec) apart. Therefore the window around each peak had to be less than 600 points for both peaks to be separated correctly. A window size of 100 points to capture each peak was chosen for the propagation delay statistical analysis.

In the channel impulse response, the LOS peak and the surface bounce peak are distinguishable as received at AMAR-A; however, the two peaks received at AMAR-B and AMAR-C were not distinguishable. This is because the LOS and surface bounce propagation delays being very close in the channel impulse responses for those distances. Using Equations (2.9) through (2.11) from Chapter 2, the geometric model was used to calculate a theoretical difference in time between the LOS peak and the surface bounce peak, the theoretical values agreed with the separation shown in the data. The time difference between the LOS and surface bounce times was confirmed to decrease as the distance increased using geometry. At farther distances, it is difficult to resolve these two propagation delays in a high-flow turbulent environment.

Figure 3.7a shows the mean LOS propagation delay at AMAR-A. Initial observations of

the LOS propagation delay plots show two cyclic behaviours in the data. The mean LOS propagation delay follows a high frequency cyclic pattern, which is the semi-diurnal tidal cycle (two high and low tides a day), and a significantly lower frequency pattern which could be related to the the spring-neap tides each month. When the water is flowing against the direction of signal propagation between the transmitter and receivers, the propagation delay should be longer than when the flow is in the same direction of the signal.

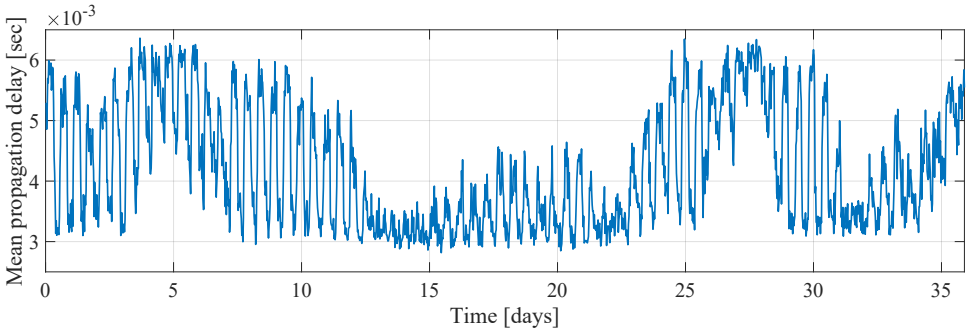

(a) Mean propagation delay

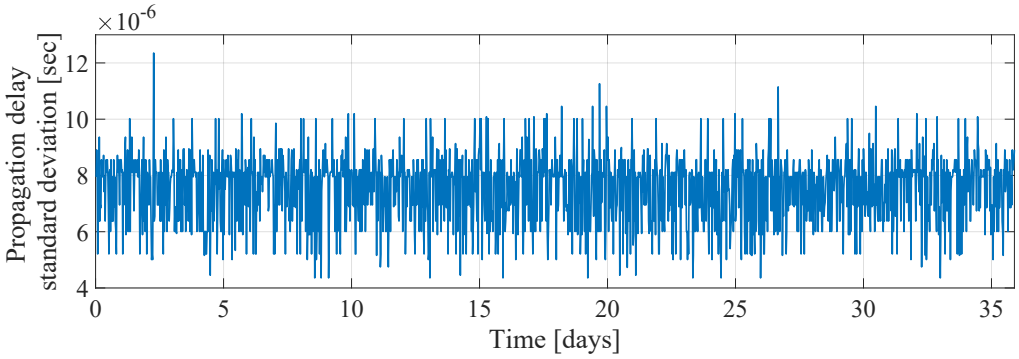

(b) Standard deviation

(c) LOS Propagation delay characteristics at AMAR-A.

Figure 3.7b shows the variance of the LOS propagation delays at AMAR-A. The variance measures the propagation delay variations for each of the 19 LFM signals. There does not seem to be any periodic patterns related to tidal flow with the LOS variance of propagation delay. The flow does not seem to have any impact on the LOS propagation delay variance.

The surface bounce mean propagation delay is shown in Figure 3.8a at AMAR-A. The mean surface bounce propagation delay is very similar to the LOS mean propagation delay. Two periodic cycles are evident, the semi-diurnal tide cycle, and the spring-neap tides.

The surface bounce propagation delay standard deviation is shown in Figure 3.8b. Interestingly, the propagation delay standard deviation is two magnitudes higher than the LOS

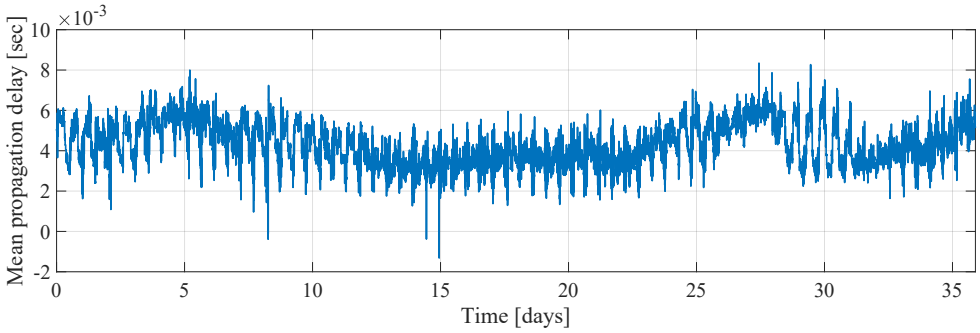

(a) Mean propagation delay

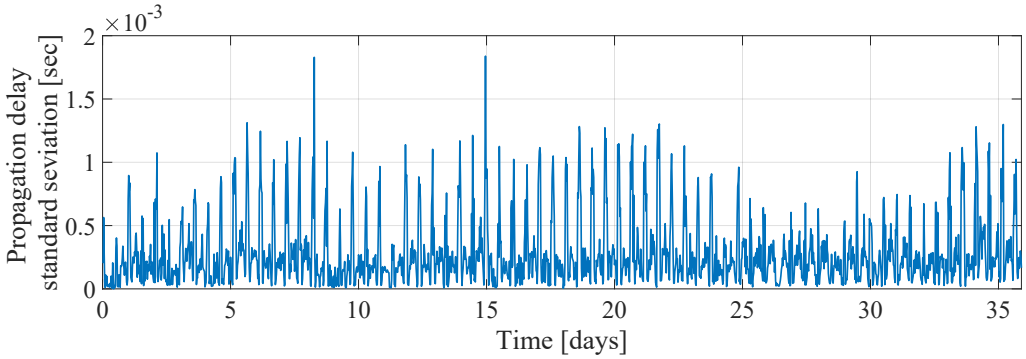

(b) Standard deviation

Figure 3.8: Surface bounce propagation delay characteristics at AMAR-A.

Table 3.3: Theoretical propagation delays from the LOS, one surface bounce and two surface bounces at AMAR-A. The time difference between the surface bounces and the LOS is denoted as $\Delta\tau$

Type of bounce	Theoretical propagation delay τ	$\Delta\tau$
LOS	49.7 msec	-
One surface bounce	59.1 msec	9.4 msec
Two surface bounces	81.0 msec	31.3 msec
Three surface bounces	108.1 msec	58.4 msec

propagation delay variance. In this case, there is a periodic cycle in the propagation delay variance. This is due to the bounce off the surface.

Observations indicate that flow has an impact on the propagation delay of the signal. The LOS and surface bounce mean flow follow a periodic cycle. The LOS and surface bounce variance of propagation delays are different. They will be analyzed in more detail in Chapter 5. Theoretical propagation delays for a LOS, a single surface bounce, two surface bounces and three surface bounces are shown in Table 3.3, assuming a nominal sound speed of 1480 m/sec at AMAR-A. The third column, denoted by $\Delta\tau$, is the difference in the propagation delays between the surface bounces and the LOS propagation delays.

Figure 3.9 shows the channel impulse response with the predicted propagation delays from the geometric model delays from Table 3.3 plotted for comparison over two days. Since the water depth is an important factor in the geometric propagation delay model, the predictions for high, low and mid- tide are shown. The plot indicates that the advection by the mean flow does have an effect on the signal arrival times. The channel geometry, driven by the changing depth due to tides, has an impact on the arrival times observed to be three orders of magnitude larger than the advection effect. There is a correlation between the arrival times of the surface reflected paths and the depth of the channel (or tide height) where, as the channel gets deeper, the propagation time increases and as the channel gets shallower the propagation time decreases.

Tables 3.4, and 3.5 show the theoretical propagation delays derived from geometry using the time, distance, and velocity relationship for AMAR-B and AMAR-C respectively. The propagation delays increase as the distance the signal travels increases; however, the difference in propagation delays between the surface bounce and the LOS decrease with increasing distance.

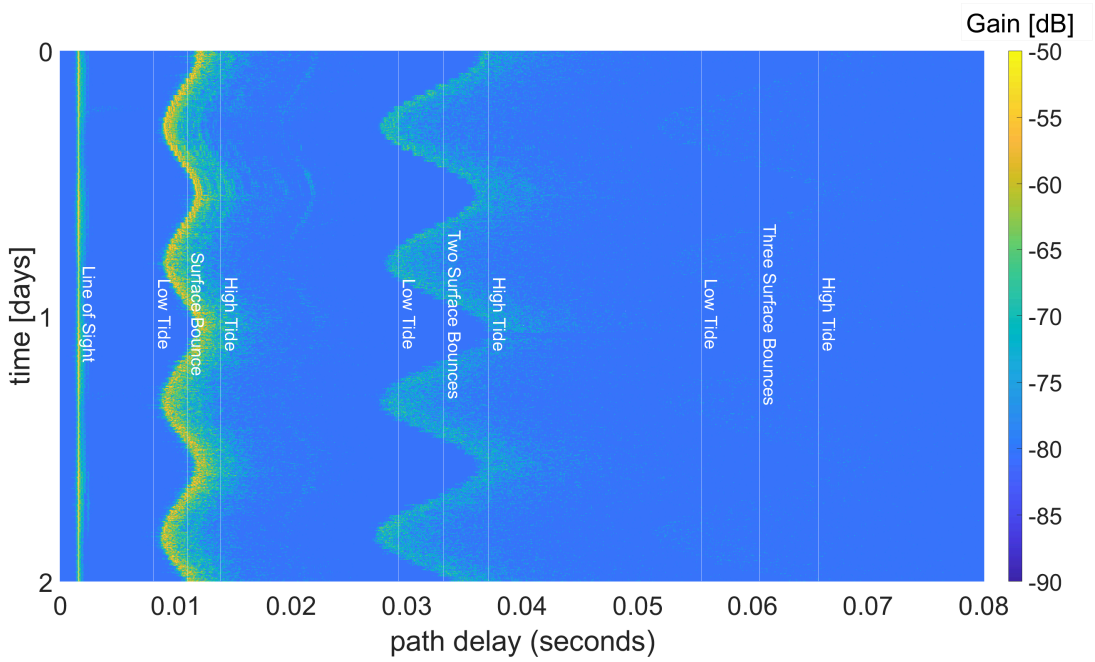

Figure 3.9: Channel impulse response showing the line of sight and the three types of surface bounces at AMAR-A. The white vertical lines indicate the theoretical values, and the color plot indicates the channel gain of the receiver signal in decibels.

Table 3.4: Theoretical propagation delays from the LOS, one surface bounce and two surface bounces at AMAR-B. The time difference between the surface bounces and the LOS is denoted as $\Delta\tau$

Type of bounce	Theoretical propagation delay τ	$\Delta\tau$
LOS	376.3 msec	-
One surface bounce	377.3 msec	1 msec
Two surface bounces	380.4 msec	4.1 msec
Three surface bounces	385.5 msec	9.3 msec

Table 3.5: Theoretical propagation delays from the LOS, one surface bounce and two surface bounces at AMAR-C. The time difference between the surface bounces and the LOS is denoted as $\Delta\tau$

Type of bounce	Theoretical propagation delay τ	$\Delta\tau$
LOS	714.9 msec	-
One surface bounce	715.1 msec	0.24 msec
Two surface bounces	715.9 msec	0.97 msec
Three surface bounces	717.1 msec	2.2 msec

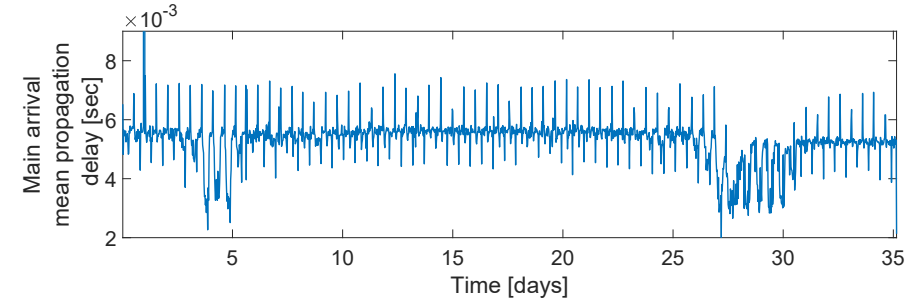

(a) Mean propagation delay

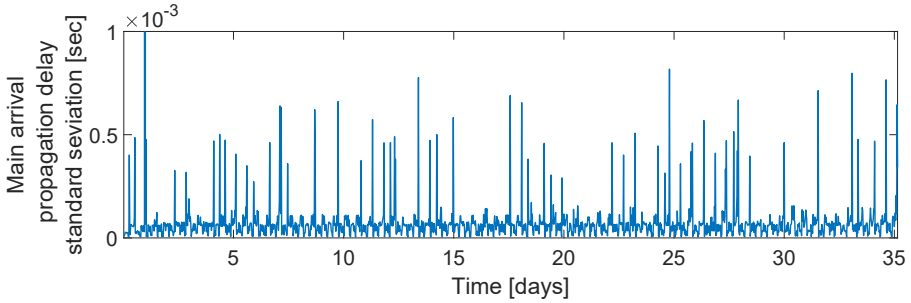

(b) Standard deviation of the delay

Figure 3.10: Propagation delay characteristics at AMAR-B.

Figures 3.10a, and 3.10b shows the mean propagation delay, and the propagation delay standard deviation at AMAR-B, and Figures 3.11a, and 3.11b represent AMAR-C. At AMAR-B and AMAR-C, a main arrival was used as a merged LOS and surface bounce propagation delay. The LOS and surface bounce signal arrive almost simultaneously at these distances.

In Figures 3.10a and 3.11a two periodic features are evident, one relating to semi-diurnal tide and the other to the spring-neap tide. In Figures 3.10b, and 3.11b the variation in the propagation delay shows periodicity which will be discussed in detail in Chapter 5. The surface bounce path has a similar changing geometry due to changing channel depth and clearly masks any change due to advection.

3.1.5 Doppler Spread

In this section, the analysis to obtain the Doppler spread will be discussed. The Doppler spread was first introduced in Chapter 2, Section 2.1.4. The signal processing uses the 10 second 8 kHz tone instead of the LFM signals to determine the Doppler spread. With the hydrophones mounted to the bottom, the Doppler spread will be minimal. Since Doppler

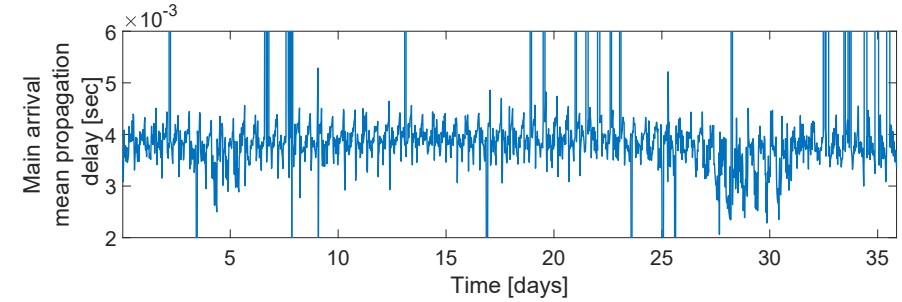

(a) Mean propagation delay

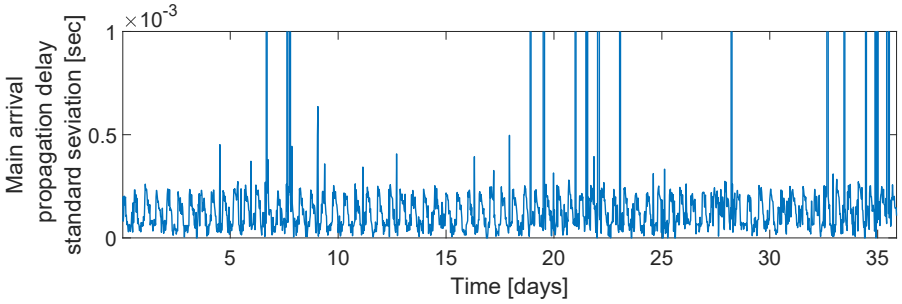

(b) Standard deviation

Figure 3.11: Propagation delay characteristics at AMAR-C.

spread increases with frequency, the highest frequency tone of 16 kHz would produce the highest Doppler spread. However, the noise floor is significantly higher at higher frequencies than it is at lower frequencies; therefore, the 8 kHz tone was used. This analysis was conducted on AMAR-B over 35 days and will determine if the tide cycle has an effect on the Doppler spread.

The signal processing for the 8 kHz tone is shown in Figure 3.12. First the tone is resampled with the same process described in section 3.1.1, using the same P/Q factor. After resampling, the signal processing of a tone requires a matched filter. The matched filter is a multiplication of the resampled data with the 8 kHz sinewave. A lowpass filter was used at base-band with a pass frequency range from 0 Hz up to 5 Hz. This filter was used to help mitigate the background noise and the mirror frequencies. Lastly, the signal was segmented into windows, each of which had eight samples N that were averaged within $r(t)$. In a free space environment, the output of the matched filter process would produce a constant signal amplitude value; however, in a fading environment the amplitude fluctuates as a function of time. The spectrum of the amplitude is used to determine the Doppler spread.

The Doppler spread is obtained by evaluating the offset frequency for which the power

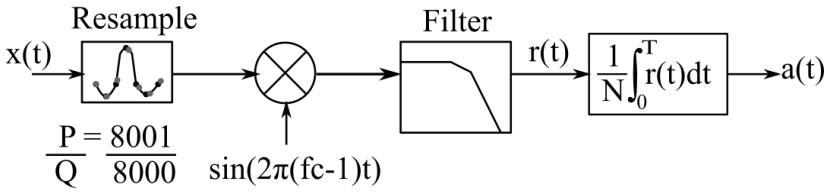

Figure 3.12: Signal processing steps applied on the recorded tone data to obtain the sequence of CIRs

spectral density falls below 3 dB from its maximum energy. To accomplish this, the channel amplitude $a(t)$ assessed over a 1-second period is represented in the frequency domain. An example of the Doppler spectrum is shown in Figure 3.13a for high, mid and low tide observations. Figure 3.13b also shows the spread of the 16 kHz signal, at high, mid and low tides and the noise floor in the 16 kHz tone is above the 20 dB value for the low tide and around the 20 dB value for the mid and high tides. As indicated above the noise floor for the 16 kHz scenario is too high to produce reliable Doppler spread assessment over the 35 days. This is attributed to the greater attenuation at high frequency. As such, in this analysis, the Doppler spread is evaluated for the 8 kHz tone.

The spread of the signal is calculated from the power spectral density (PSD) of the matched filter output signal $a(t)$. The Welch PSD method was used due to the increased reliability of the measurements over the periodogram method [40, 41]. The Welch PSD estimate improves with an increasing amount of data, whereas the periodogram estimate remains the same. The resolution was determined by having a non-uniform fast Fourier transform (NFFT) size of 32768 to get a resolution of approximately 0.2 Hz. This frequency resolution will capture the Doppler spread where as having a resolution higher than 1 Hz will not capture the Doppler spread. The next step was to find the 3 dB spread off the maximum energy around the carrier frequency of 8 kHz. The results of the Doppler spread can be seen in Figure 3.14a.

Figure 3.14a shows that the Doppler spread fluctuates around 0.25 Hz, at times reaching beyond 0.3 Hz. The Doppler spread was also calculated using the 20 dB spread, off the main peak, shown in Figure 3.14b. A threshold of 20 dB is chosen for comparison purposes, because it is found that the standard definition of the 3 dB cutoff for the Doppler spectrum is smaller than the 0.2 Hz resolution defined by the Welch PSD. Comparing the two figures, the Doppler spread from the 20 dB spread varies significantly when compared to the Doppler spread from the 3 dB spread. In addition in Figure 3.14b, the Doppler spread fluctuates

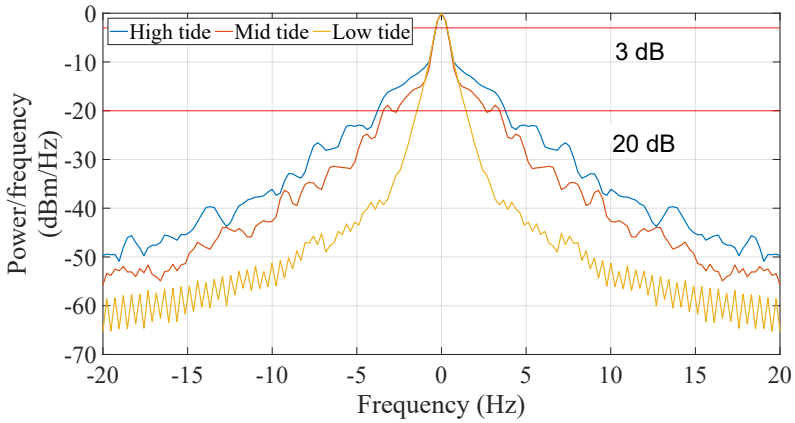

(a) Frequency of 8 kHz

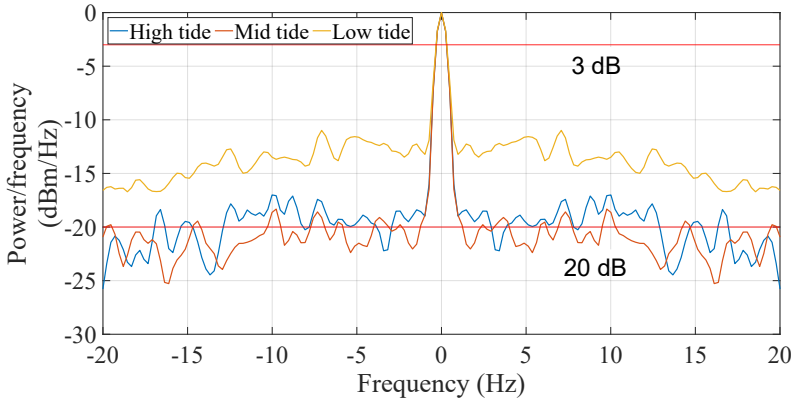

(b) Frequency of 16 kHz

Figure 3.13: Power spectral density of the signal $a(t)$.

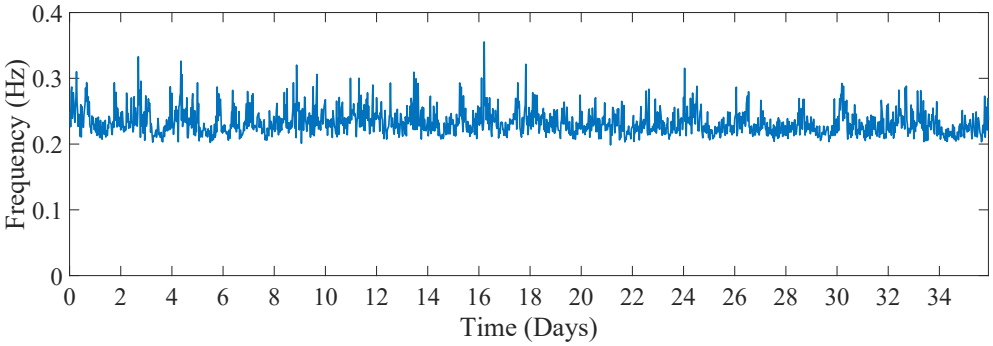

(a) Measured using the standard 3 dB cutoff frequency.

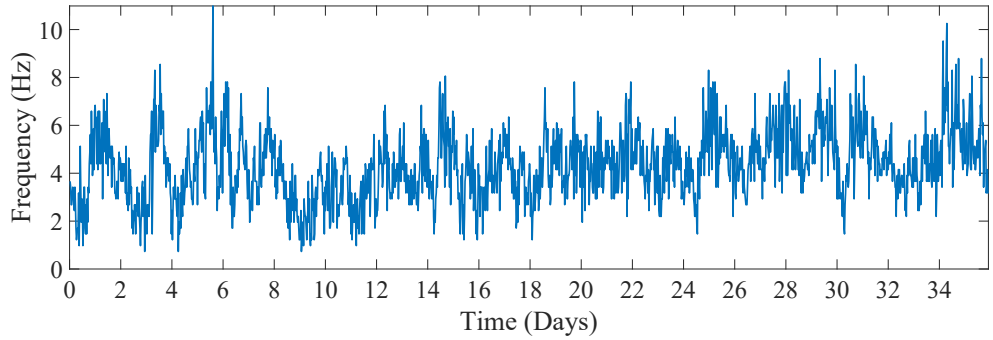

(b) Measured using a wider 20 dB cutoff frequency.

Figure 3.14: Representation of the Doppler spread evaluated for all tide cycles.

around 4 Hz, and reaches as high as 9 Hz at certain times. Note that the quantitative values measured for the 20-dB cutoff are much larger than expected in theory, and this result is simply used to determine whether a trend can be observed as a function of tide cycle.

Using the Doppler spread of the signal sampled every 30 minutes over all 35 days, the PSD of the Doppler spread measurements is calculated, as shown in Figure 3.15. A tone in the spectrum of the Doppler measurement shows a frequency of 1.9 cycles per day or 1/12.5 cycles per hour, which again corresponds to the tide cycle. This shows that the Doppler spread has energy at the semi-diurnal frequency.

3.2 Flow and Tide Data Analysis

The ADCP flow and pressure logger provided only 14 days of data. An extrapolation method was required to predict the flow and tide height over the entire 35-day sea trial. The data recorded was from the first 14 days, and the flow and tides for the remaining 21 days were extrapolated from the data. The recorded flow speeds and the recorded tide levels from the

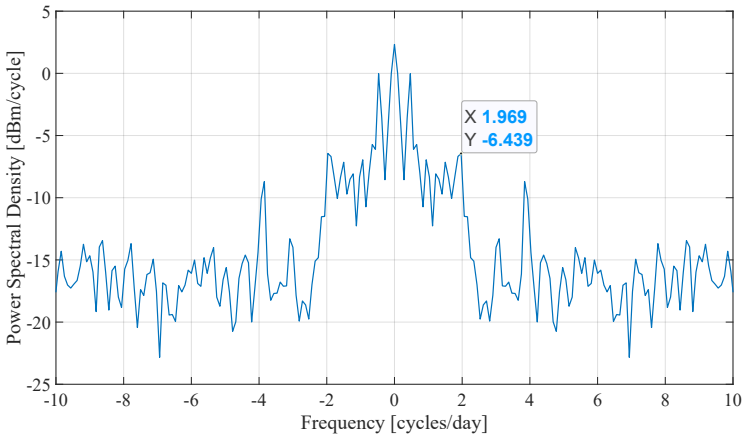

Figure 3.15: Power spectral density of the Doppler spread.

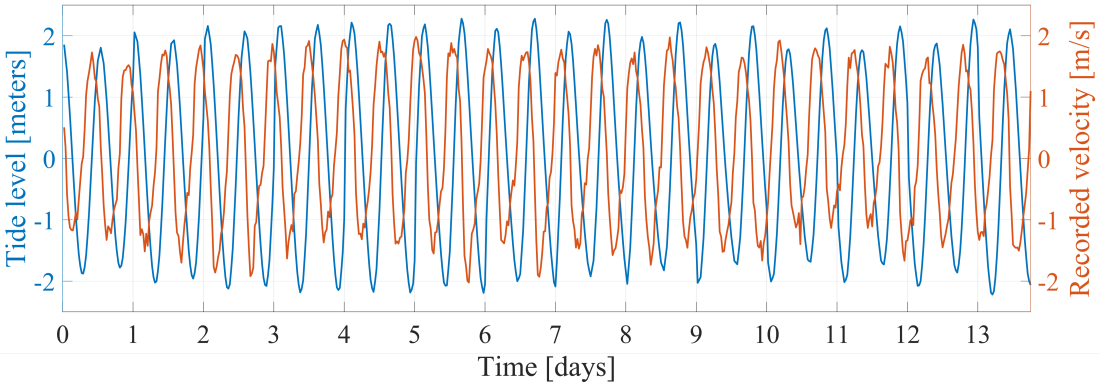

Figure 3.16: Recorded tide levels and flow speeds.

ADCP data plotted over the first 14 days are shown in Figure 3.16. When the tide level is at its minimum or maximum, the flow speed is close to zero. The flow speed is at a maximum value when the tide level is at roughly the midway point between the high and low values. This indicates the tide level and flow speed are out of phase by 90 degrees.

The extrapolated flow velocity was calculated from the differential tide height, Δh. The amplitude was scaled up three times from its original size to fit the recorded data. The data on the tides for the remaining 21 days came from TPXO9-atlas [42]. This differential tide height relationship was compared to the recorded flow velocities to determine if the extrapolated flow velocities have the correct phase relationship. A plot of the differential tide height and the ADCP recorded flow speeds is depicted in Figure 3.17. Figure 3.17 shows that the phase relationship between the differential tide height and the recorded ADCP flow

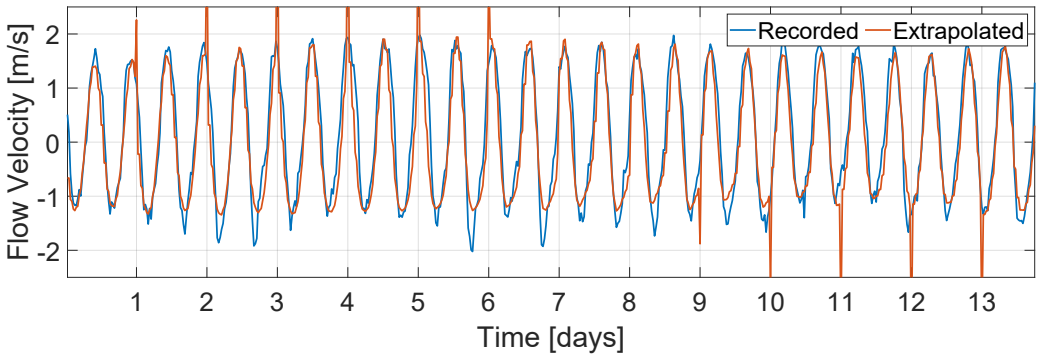

Figure 3.17: Recorded flow speeds and differential tide height.

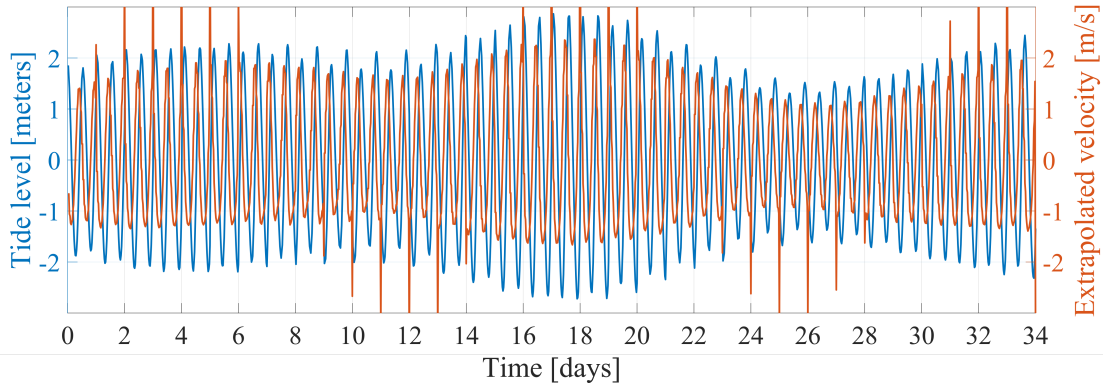

Figure 3.18: Extrapolated flow speeds against tide level.

speeds are similar, making the differential tide height a valid way to extrapolate the velocity over the remaining days. The extrapolated flow over all 35 days is plotted against the tide level in Figure 3.18. The extrapolated flow is denoted as the differential tide height represented as the orange line. The tide level is represented as the blue line. The phase relationship between the extrapolated flow and tides agrees with the recorded tide level and flow speeds relationships.

Figure 3.19 shows the relationship between the mean flow and the standard deviation of the flow. The ADCP recorded the flow speeds in three directions; north, east and vertical over the depth of 20 meters. The magnitude of the three directions of flow speeds is calculated using the ebb tide as the positive direction and the flood tide as the negative direction. As the data is sampled every five minutes, a single flow value is obtained every 30 minutes from computing a mean and standard deviation on six flow samples. Figure 3.19 shows the empirical relationship between the mean and standard deviation of the flow. It can be seen

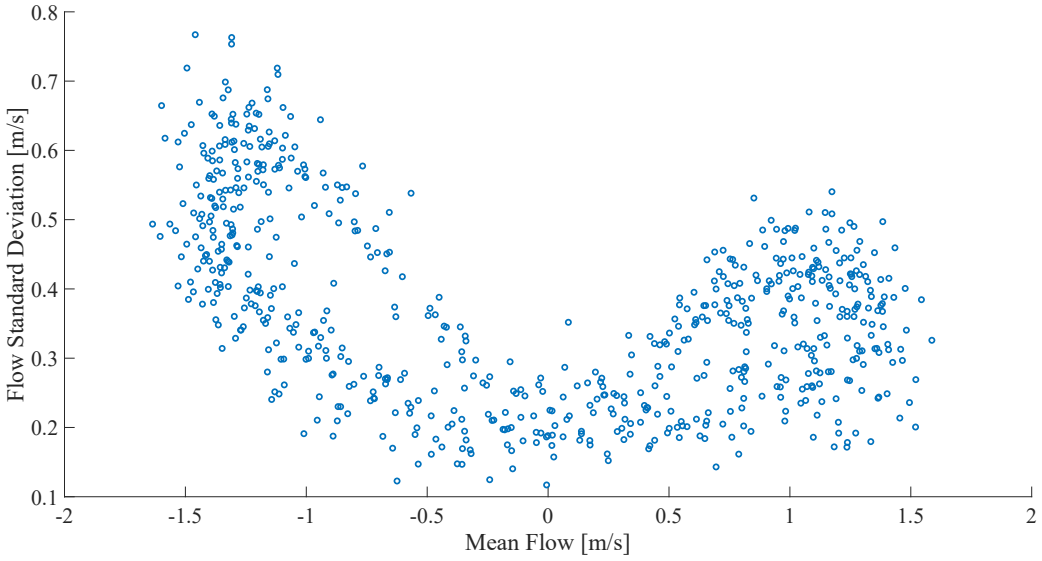

Figure 3.19: Mean flow versus flow standard deviation.

that the flow variance increases with increasing mean velocity.

3.3 Chapter 3 Summary

This chapter reviewed the data analysis to determine the channel characteristics. This included channel gain, delay spread, Doppler spread, and time of arrival. The process involved resampling the signal, filtering the signal, down converting it to base-band, and using a LFM reference signal to determine the channel impulse responses with a cross-correlation. From here, the estimate of the channel impulse response was used to determine the channel gain, delay spread, and propagation delay characteristics. The Doppler spread was obtained from the signal processing on the 8 kHz tones. In addition, the ADCP measured flow velocity and tides were only recorded for the first 14 days, and were extrapolated over the remaining 21 days.

Initial observations revealed that tides have an impact on the channel characteristics. The high speed flows from the tides create a communication link between the transmitter and receiver that fluctuates over time with a cyclic behaviour. The flows add and subtract as a vector to the sound speed, which may effect the latency of the link depending on the direction of flow. The tidal cycle can be seen in data and will be covered in more detail in Chapter 5.

Chapter 4

Modelling Channel Characteristics in the Bay of Fundy

In this chapter, two complimentary procedures used to model the channel characteristics are presented. Specifically; in Section 4.1, the background information on the ray tracing algorithm is discussed, and a description of the Bellhop simulator is included; in Section 4.2, a model relying on stochastic processes is configured to model the effect of surface roughness and tide height on the acoustic signal; finally, in Section 4.3, the effect of variable mean flow and turbulence is modelled using a ray tracing simulator with a range dependent sound speed.

4.1 The Ray-Tracing Algorithm

The ray tracing algorithm models the acoustic rays propagating through an underwater environment. According to [28], the ray tracing algorithm is derived from mathematical ray-based models, and ray theory which originally emerged from reflection and refraction in optics.

Bellhop is a ray tracing algorithm that is available at no cost and is implemented within Matlab. The library, developed by Porter and Liu [28], outputs the complex acoustic pressure field from which transmission loss may be computed as well as pressure amplitudes and travel times when provided environmental conditions as inputs.

Ray theory and the Bellhop ray tracing algorithm will be presented in the next two sections. In Section 4.1.1, a high level discussion of the theory to derive the eikonal and transport equations and their solutions is included; finally, in Section 4.1.2, the setup for the Bellhop ray tracing algorithm developed by Porter and Liu [28] is discussed.

4.1.1 Ray-Tracing

In this section, a high level fundamental review of ray tracing is discussed to provide insight into how the Bellhop ray tracing algorithm works. Ray-tracing is a method for calculating the path taken by a wave as it propagates through an environment that takes into consideration

the varying sound speed and boundary conditions. Specifically, a wave that propagates outwards from a source in all directions, produces wave-fronts that can be represented as spheres around the source. Lines that are normal to the wave-fronts in specific directions are considered rays. It is assumed that the specific part of the wave will propagate in the direction of the traced ray.

When rays hit a boundary some of the wave energy will reflect off the boundary and some of the energy will refract into the boundary. The reflection and refraction of rays at a boundary can be described with Snell's law, explained in Chapter 2. Snell's law determines both the reflected angle and refracted angle of the ray. The path that the ray takes is calculated using the the Helmholtz equation, which stems from a solution to the wave equation. Depending on the type of wave, the path the ray takes requires initial conditions such as the direction and its position in space. A particular scenario of ray-tracing is used in underwater acoustics.

Applied to underwater acoustic propagation, a ray is based on the assumption that it is a line drawn normal to the acoustic wave front as it propagates in a specific direction. A typical underwater environment can be described as a two-dimensional waveguide with an air-sea surface boundary and a bottom boundary. The speed of sound in the underwater environment is defined from a depth dependent sound speed profile. The speed of sound in the sea is dependent on temperature, salinity, and pressure of the ocean. It is assumed that the air-sea interface is a perfectly reflecting boundary while the bottom boundary has different reflection properties depending on the seabed characteristics. The wave will propagate through various regions of sound speed depending on the ocean characteristics which causes the wave to refract away from regions of higher sound speed. Snell's law is used to determine the refracting behaviour of the ray.

The ray tracing algorithm in an underwater environment uses the Helmholtz equation and the acoustic pressure field to produce a system of equations known as the eikonal equation and the transport equations [28]. The eikonal equation relates the delays τ to the sound speed c. In addition, the eikonal equation is solved to calculate the ray paths, from which the delays τ can be computed in seconds. The transport equations are used to calculate the energy carried by the rays (or pressure amplitudes), $a(\tau)$ in Pascals and phase along each ray in space. This information will produce the channel impulse response, and transmission loss estimates as a function of depth and range.

4.1.2 Bellhop

In this section, a review of how to use the Bellhop library in Matlab is presented. This will include the set up of the input files. An explanation of each input file is presented, followed by the outputs of the algorithm.

To use the Bellhop ray tracing algorithm, the appropriate environment should be configured. This environment requires two input files: a SSP file and an environment file with a specified depth. Optionally, a bathymetry file may be used to simulate the ocean floor. The bathymetry file includes information on the depth of the ocean floor as a function of range along the propagation path. The bottom compositions are specified as sound speeds in selected materials such as gravel, sand and others, inside the environment file. The air-sea interface is at zero meters. An SSP file gives the sound speeds at specified depths. Bellhop can also use a range dependent SSP where the sound speed is a function of depth and range. Finally, the environment file is an instruction file that provides input parameters to the Bellhop script. In addition, other settings such as transmitter and receiver depths and the take off angle ranges are required to complete the input files.

To produce the transmission loss, Bellhop can be configured in three different modes: coherent, incoherent and semi-coherent. Coherent transmission loss outputs a very detailed interference pattern which is typically not measurable, and as its name implies, it coherently adds all the path arrivals to form the transmission loss. Incoherent transmission loss smoothens out the detailed interference pattern by ignoring the phase, and can be stable even at higher frequencies. The semi-coherent transmission loss is essentially an approximation between the coherent transmission loss and the incoherent transmission loss. Ideally, the semi-coherent transmission loss retains some features insensitive to detailed interference patterns but smoothens out the features that are not measurable.

When the Bellhop ray tracing environment is set up in this work, the bathymetry file is representative of the bathymetry of a two dimensional slice of the Grand Passage bathymetry as shown in Fig 2.9. The settings in the environment file are set to use a range dependent SSP, that will allow for modelling the effect of flow and turbulence. The ray tracing algorithm outputs multiple file types; however, the main output files are the ray tracing, propagation delay, and transmission loss plots. Alternatively, Bellhop can be configured to produce a propagation delay plot that shows the pressure amplitude and the propagation delay between the transmitter and receiver. The propagation delay plots will be used to model the

propagation delay statistics in Section 4.3.

4.2 Effect of Surface Roughness and Tide Height

In this section, a stochastic channel model that can be used to account for the effect of time variance in an underwater acsoutic channel is presented. The model, originally described in [29] uses at its core the deterministic acoustic ray-tracing algorithm, which is enhanced with a set of random processes to model the channel impulse response variations under different conditions. Note that in [43], it was configured to assess the ability of predicting the channel in environments with time varying physical parameters. Here, the propagation model is applied to the proposed deployment scenario to describe the acoustic properties as a function of time-varying water depth, and surface roughness.

As demonstrated in [29], to model the time-varying channel during a period of T, at a particular realization time $t_n \in T$, its frequency response H can be expressed as:

$$H(f, t_n) = \sum_p h_p(t_n)\tilde{\gamma}_p(f, t_n)e^{-j2\pi f\tau_p(t_n)}, \tag{4.1}$$

where, for each path p at time t_n, $\tilde{\gamma}_p(f, t_n)$ is the small-scale path coefficient that models the effect of Doppler spread at frequency f. It is derived using $\tilde{\gamma}_p(f, t_n) = \gamma_p(f, t_n)e^{j2\pi a_p f t_n}$, where a_p is the Doppler factor for path p.

When the signal at the receiver is subject to multiple echos, discrete path delays $\tau_p(t)$ and path gain $h_p(t_n)$ introduce frequency selectivity. For each path p, the delay $\tau_p(t_n)$ is time-dependent. In practice, the channel path delays are bundled in clusters of rays, and the scattering coefficients for each discrete cluster of paths follow a Gaussian distribution.

Among the different phenomena, the effect of the tides shown in Figure 4.1 on the channel gain and delay spread will be evaluated over the course of a lunar cycle.

For the model developed in this section, the SSP is assumed to be approximately constant as a function of depth and range because of the high rate of vertical mixing in the channel. Nonetheless, it varies as a function of time throughout the day, and at different periods of the year, due to temperature variation. In the period of time during which the measurements were taken, the average daily water temperature varies between 13.8 °C and 16.6 °C. The bottom consists of gravel from the source to AMAR-B, and is modelled using an acoustic-elastic half-space with $c_b = 1800$ m/s.

The stochastic simulator is utilized to produce a sequence of channel impulse responses (CIRs) $h(t_n, \tau),\ t_n \in T$. Once the estimated sequence of CIRs is obtained, it can be analyzed using multiple channel metrics to get a better understanding of the channel properties and their impact on the acoustic communication.

To simulate the channel gain, the sequence of CIRs at the output of the ray tracing simulator is converted in the frequency domain as in (4.1). Since the channel $H(f, t_n),\ t_n \in T$ is frequency selective, the overall channel instantaneous gain $G(t_n)$ at time t_n can be calculated from

$$G(t_n) = \frac{1}{B} \int_{f_0}^{f_0+B} |H(f, t_n)|^2 df, \tag{4.2}$$

where $B = 8000$ Hz is the bandwidth and $f_0 = 8000$ Hz is the lower cutoff frequency.

Figure 4.1 depicts the variations of the channel instantaneous gain and RMS delay spread simulated over a period of 24 hours. As can be observed, the channel gain is approximately in antiphase proportional to the tide level.

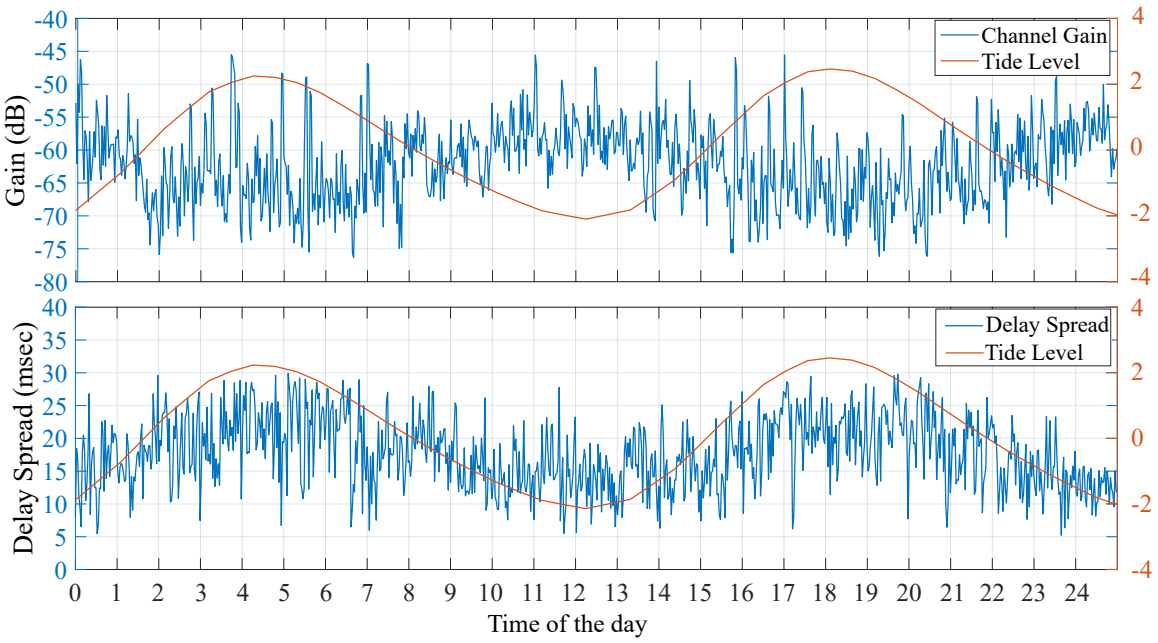

Figure 4.1: Channel gain and delay spread simulated by the stochastic model for Sep. 28$^{\text{th}}$, 2018.

From these results, in Figure 4.2 the probability density functions (PDFs) of the instantaneous channel gain $G(t)$ and RMS delay spread $\tau_{RMS}(t)$ are evaluated for the deployment

scenario in Grand Passage. From the analysis of the PDF of the RMS delay spread shown in Figure 4.2, the RMS delay spread tends to increase at high tide and reduce at low tide. Also, the channel gain has more variance at high tide which results in frequency-selective fading.

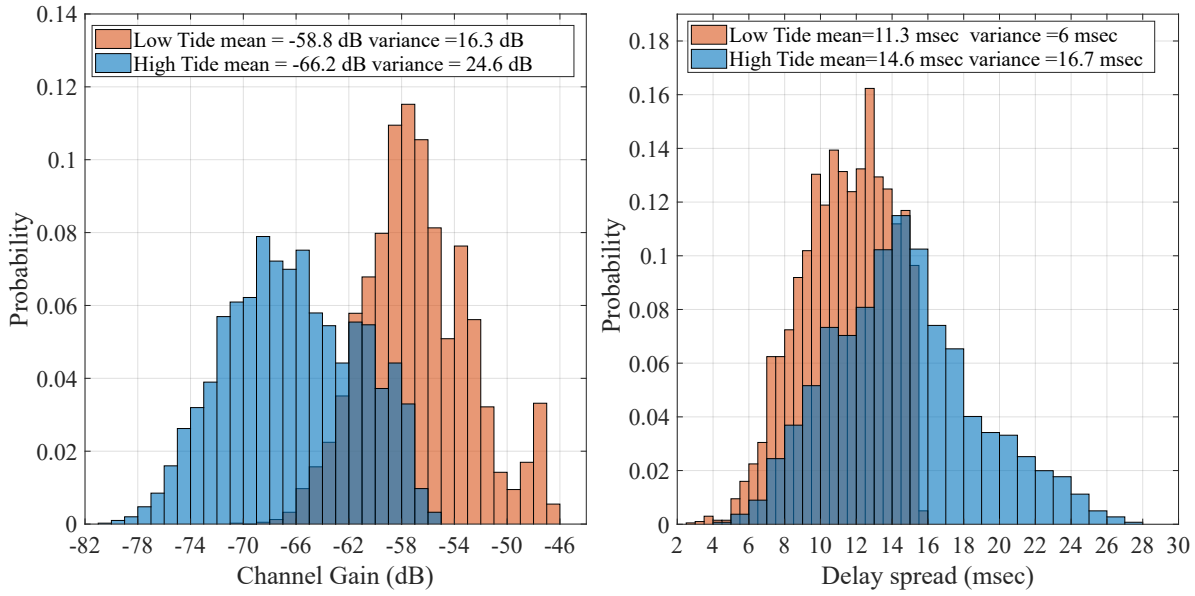

Figure 4.2: PDFs of the channel gain and delay spread simulated by the stochastic model for Sep. 28$^{\text{th}}$, 2018.

The most probable value for the channel gain is -58.8 dB during the low tide time period of 11:00 to 12:00 and -66.2 dB during the high tide period of 17:00 to 18:00 on Sep. 28$^{\text{th}}$, 2018. Accordingly, the most probable value for the RMS delay spread is 11.3 msec during the low tide and 14.6 msec during the high tide. The PDF's of the measured channel gain and delay spread measurements will be discussed in Chapter 5, Section 5.3.

In this section, the effect of flow is not taken into consideration in the modelling of the propagation signal. In the next section, flow will be modelled by adding the mean and turbulent flow velocity to the acoustic sound speed, giving a variable sound speed as a function of range and time. It will be shown how the flow impacts the variance of the channel propagation delay.

4.3 Modelling Turbulence with Range Dependent Sound Speeds

This section presents a technique to model the effect of mean flow and turbulence on the LOS acoustic signal by building a turbulence model with the Bellhop algorithm. First, the configuration of the Bellhop algorithm to represent the deployment scenario in the Grand Passage experiment is described. Following this, the output of the turbulence model, consisting of the effect of turbulence on the propagation delay variance is evaluated.

Bellhop is configured to represent the deployment scenario represented in the Grand Passage experiment. First, the bathymetry file, obtained from JASCO Applied Sciences, was set up to match the bathymetry in the Grand Passage between the transmitter and the receivers. However, the Bellhop bathymetry file is only able to show a two-dimensional cross section of the bathymetry. A plot of the transmission loss and the bathymetry was obtained throughout the channel. The following analysis is realized for AMAR-A and AMAR-B as the model for AMAR-C does not have a LOS path due to a bathymetric feature, as shown in Figure 4.3.

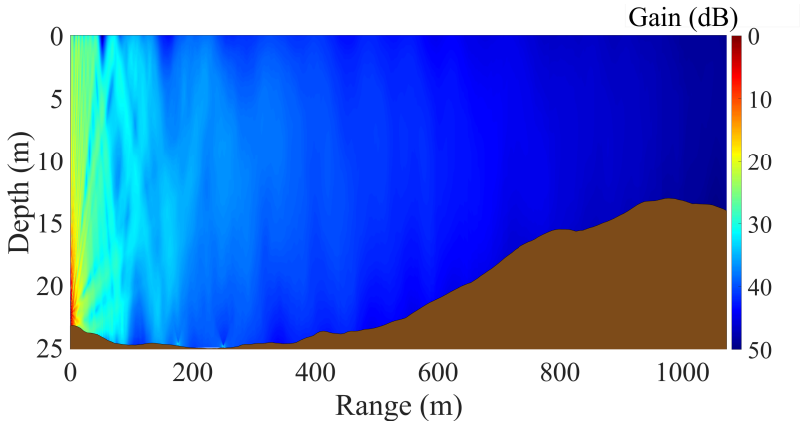

Figure 4.3: Transmission loss simulation showing the bathymetry of the acoustic channel.

The acoustic channel is shallow between the transmitter and receivers, ranging from 24 meters at the deepest point, to 13 meters at the shallowest point. The sound speed is assumed to be on average equal to 1480 meters per second across the water column. The range dependent SSP will be used to simulate both the mean flow, $\overline{c_f}$, and turbulent flow, c'_f. In addition, a decay coefficient α parameter is used to control the relative size of flow regions in the channel.

The procedure to assess the impact of turbulence and flow on the propagation is depicted

in Figure 4.4 below in a flow chart format. To represent the effect of advection of acoustic signals by the turbulent flow, a range dependent SSP matrix is defined to vary as a function of depth and range. To model the effect of turbulent flow on the propagation delay of the signal, a random flow velocity perturbation is added to the speed of sound at all points along the propagation path. As such, for a given mean flow value $\overline{c_f}$, 100 sound speed realizations are produced, each representative of an instance of the given turbulent flow conditions corresponding to the mean flow. From Figure 3.19 the standard deviation of flow tends to increase linearly with the absolute value of its mean, albeit with different slopes. The Bellhop simulator computes the acoustic field, for each random realization of turbulent flow. The delay of the first path arrival is recorded for each observation. The variance over the 100 realizations is then computed for that given mean flow $\overline{c_f}$. This is repeated for six mean flow speeds from 0 to 2.5 m/sec.

To represent local turbulence regions with realistic spatial statistical properties, a two-dimensional finite impulse response (FIR) filter is used to create a normalized correlation matrix $\mathbf{R_{norm}}$. For this purpose, a decay coefficient, α with units of meters^{-1} is introduced. The decay coefficients K_z for the FIR filter as a function of depth Z in meters are calculated to be $K_z = e^{-\alpha Z}$, while the coefficients K_r as a function of range R in meters are calculated to be $K_r = e^{-\alpha R}$ matrices. In fact, the FIR filter is used to produce a normalized correlation matrix $\mathbf{R_{norm}} = \mathbf{R}/\mathrm{E}[\mathbf{R}]$. A random uncorrelated normal sound speed matrix is generated with a variance determined by its empirical relationship to the mean flow speed and then filtered by the correlation matrix $\mathbf{R_{norm}}$ to generate the depth and range dependent sound speed matrix. By adjusting the decay coefficient α, regions of turbulence with different correlation length-scales can be created.

Two realizations of turbulent flow are shown in Figure 4.5 for a nominal sound speed of $c = 1480$ m/sec. As can be observed, a small decay coefficient $\alpha = 0.1$ m^{-1} will lead to large regions in which the turbulent advection remains relatively constant, while a very high decay coefficient $\alpha = 10$ m^{-1} will give small scale turbulence, c'_f throughout the channel.

In this work the first propagation delay in the simulated channel impulse response is used to represent the LOS path. It should be noted that the varying SSP as a function of depth introduces reverberation. Figure 4.6a shows the output of the model where each data point is computed from an ensemble of 100 realizations. The model uses a zero mean flow, each with a randomly generated turbulent advection velocity added to the SSP.

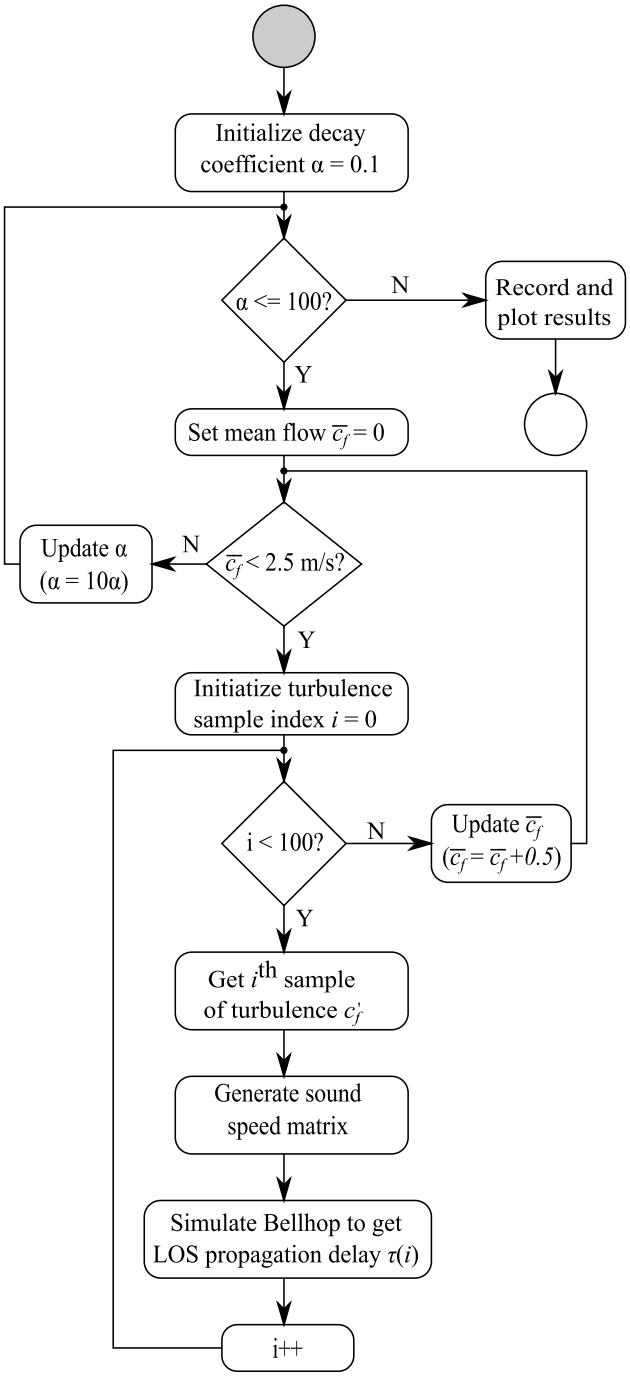

Figure 4.4: Turbulence model flow chart

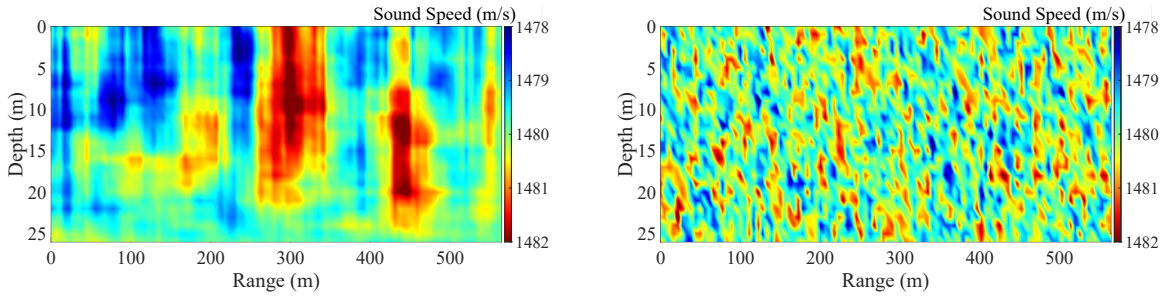

(a) Decay coefficient $\alpha = 0.1$ (b) Decay coefficient $\alpha = 10$

Figure 4.5: Representation of the range dependent sound speed as a function of range and depth for AMAR-B.

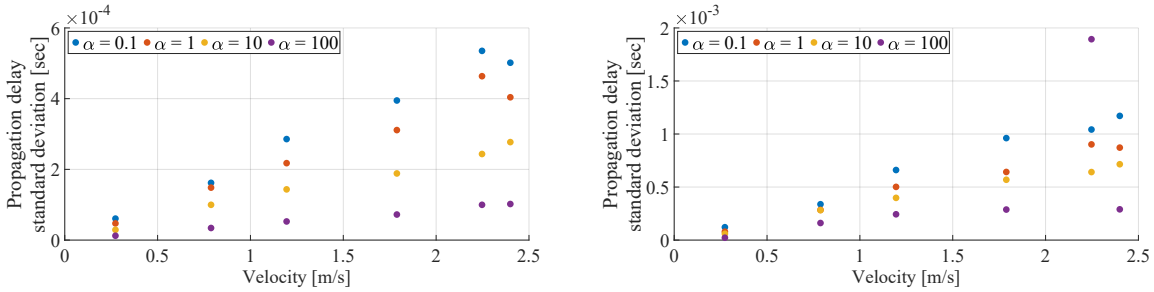

(a) AMAR-A (b) AMAR-B

Figure 4.6: Standard deviation of propagation delay versus flow velocity for different decay coefficients.

Figures 4.6a, and 4.6b confirms that the propagation delay standard deviation increases linearly with mean flow speed, and thus with turbulent flow speeds. The model is configured with four different decay coefficients that indicate the spatial correlation of the turbulent advection sound speed perturbation. The plot shows that for low decay coefficients, the standard deviation of propagation delay is larger, in comparison to when the decay coefficient is large. This confirms that when large eddies dominate the turbulent flow field, the propagation delay of the LOS can be subject to more small-scale variation at each given tide level. In addition, the larger distance of AMAR-B gives a larger variability in the propagation delay than the AMAR-A distance. As such, this indicates that the longer the distance an acoustic signal travels, the larger the variability of the propagation delay on the LOS path.

4.4 Chapter 4 Summary

This chapter focused on modelling the effect of flow on the channel characteristics in the Bay of Fundy. First the set up of the Bellhop algorithm developed by Porter and Liu [28] was discussed. Bellhop uses the equations from [28] to build a ray tracing algorithm capable of predicting the acoustic propagation. Set up files include an environment file, a bathymetry file, and a SSP to allow the algorithm to be executed.

Next the channel gain and delay spread were modelled over 24 hours on September 28^{th}, 2018. The model predicted that the channel gain had an inversely proportional relationship to the tide level, whereas the delay spread followed the tide level.

Finally, the effect of turbulence on the variability of the propagation delay for the LOS path was discussed. Building on Bellhop's propagation delay outputs, a random range dependent SSP was used to model turbulent regions. A decay coefficient, α was used to simulate large and small regions of turbulence. Results show that as the flow increases, so does the time of propagation delay variability, and larger regions of turbulence also lead to high propagation delay variability.

Chapter 5

Effect of Flow on the Measured Channel Characteristics in the Bay of Fundy

In this chapter, the acoustic channel characteristics are analyzed as a function of mean flow, using measurements taken during the sea trial. Specifically; in Section 5.1, the effect of mean and turbulent flow on the mean and standard deviation of the channel gain are presented; in Section 5.2, the effect of mean and turbulent flow on the mean and standard deviation of the delay spread are explored; in Section 5.3, the LOS and surface bounce propagation delays for AMAR-A are assessed; finally, in Section 5.4, a summary of the chapter is presented.

5.1 Channel Gain

The channel gain represents the received signal power as a function of the transmit power. In basic terms, the channel gain is determined as the ratio of the received signal to the transmitted signal. The channel gain is represented in decibels for 10 channels in total. Four channels each for AMAR-A and AMAR-B and two channels for AMAR-C. There are 19 channel gain values calculated on each of the 10 receiver channels.

Consecutive measurements were taken over a 35 day period for the 10 receiving channels at the three distances. To evaluate the impact of mean flow, a statistical analysis on the channel gain was calculated based on 19 samples over each 30 minute period to produce a mean $20\log\overline{CG}$ and standard deviation $10\log(\mathrm{STD}(CG))$ of the channel gain. This is shown for five days in Figures 5.1a, 5.1b, and 5.1c. The mean is plotted as the blue line, and the standard deviation is plotted as a grey region around the mean channel gain. As can be observed, the average channel gain is approximately -35 dB for AMAR-A, -55 dB for the AMAR-B, and -60 dB for AMAR-C. The standard deviation of the channel gain from each of the 10 channels is approximately $\pm$10 dB on either side of the mean channel gain. One trend that can be observed is when the standard deviation is low, the mean channel gain is high, indicating that high temporal variability in the channel degrades the overall channel gain. By computing the frequency spectrum of the time series, the fundamental frequency

is found at $1/12.5 = 0.08$ cycles per hour, or near the primary tidal frequency. This can be seen in a power spectral density of the mean channel gain in Figure 5.2a and channel gain standard deviation in Figure 5.2b.

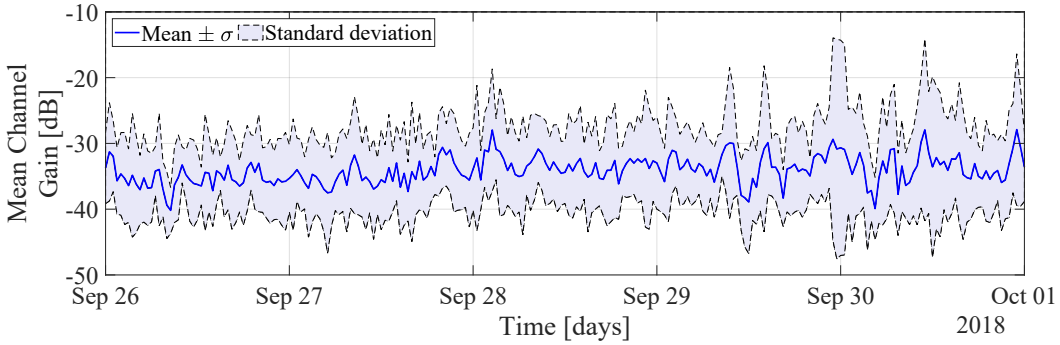

(a) AMAR-A

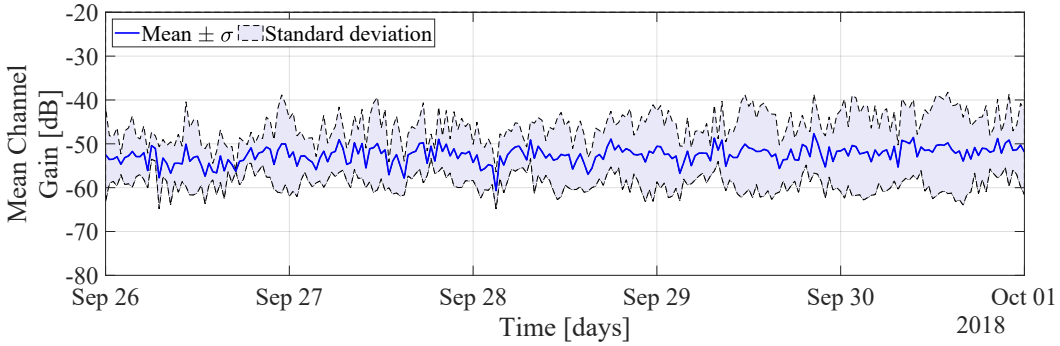

(b) AMAR-B

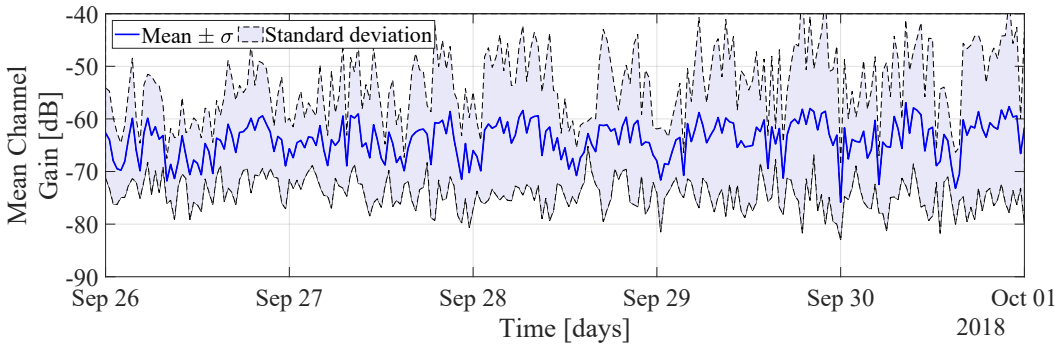

(c) AMAR-C

Figure 5.1: Statistical channel gain over five days from nine up signals and 10 down signals.

To obtain further insight on the impact of mean flow on the channel gain, the tide height against the mean channel gain was plotted. This is shown below in Figures 5.3a, 5.3b, and 5.3c where the blue points represent the mean channel gain, the red line is a linear fit and the grey region represents the standard deviation of the channel gain. To obtain as

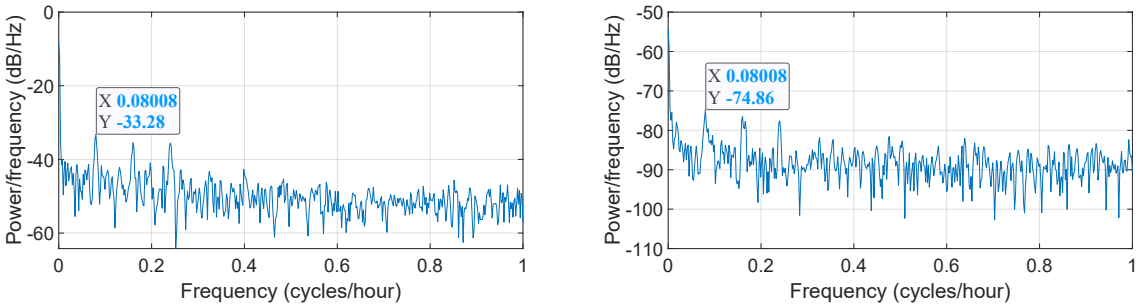

(a) Power spectral density of the mean channel gain

(b) Power spectral density of the channel gain standard deviation

Figure 5.2: Power spectral density for one channel on the mean and standard deviation of the channel gain at AMAR-A.

many samples as possible, the mean channel gain and standard deviation over all 35 days and for all 10 channels were used.

In Figures 5.3a, 5.3b, and 5.3c, as the tides are transitioning between low and high, the flow of the water is at its maximum. In Chapter 4, the mean channel gain for AMAR-B was modelled in antiphase with the tide cycle. To agree with this channel gain model, the linear fit of the mean channel gain should be a negative slope from low tide to high tide. Referring to Figure 5.3b a slight negative slope for AMAR-B is evident. In Figure 5.3a a negative slope is evident for AMAR-A. In Figure 5.3c a positive slope is evident for AMAR-C. This is attributed to the fact that the the receiver at AMAR-C is behind a bathymetric feature. In this condition, a surface reflected path with a smaller incident angle with respect to the normal occurs at high tide, which is less sensitive to sea surface roughness, thus a higher channel gain at high tide might be expected. Note that the standard deviation of the channel gain (in light gray) follows the same trend as the mean value. The following section will analyze the effect of mean and turbulent flow on the delay spread.

5.2 Delay Spread

In this section, the mean and standard deviation of the delay spread are analyzed. The delay spread is calculated using the channel impulse response produced using the LFM probes, and evaluated for the 19 probing sequences at each half hour. The results of a representative window of 35 days are shown in Figures 5.4a, 5.4b, and 5.4c. Similar to the channel gain, a mean and standard deviation of the measurements for each 30 minute interval is taken to

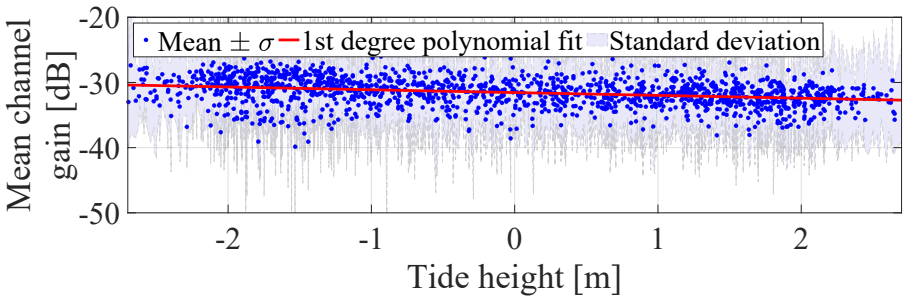

(a) AMAR-A

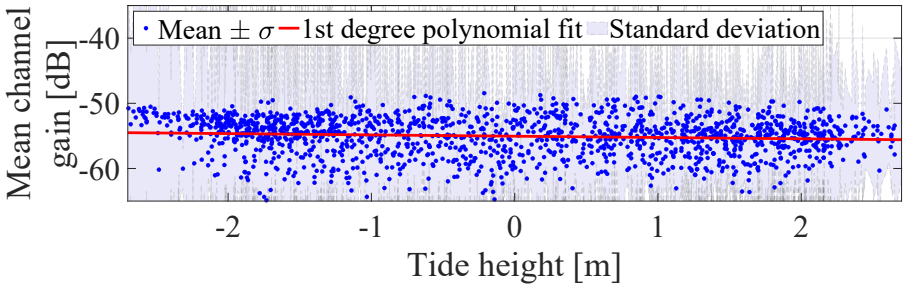

(b) AMAR-B

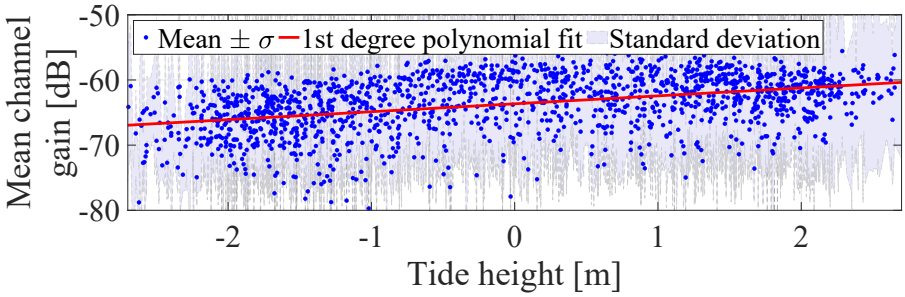

(c) AMAR-C

Figure 5.3: The figure shows the mean channel gain over all the days versus the height of the tides.

analyze the effect of the mean and turbulent flow.

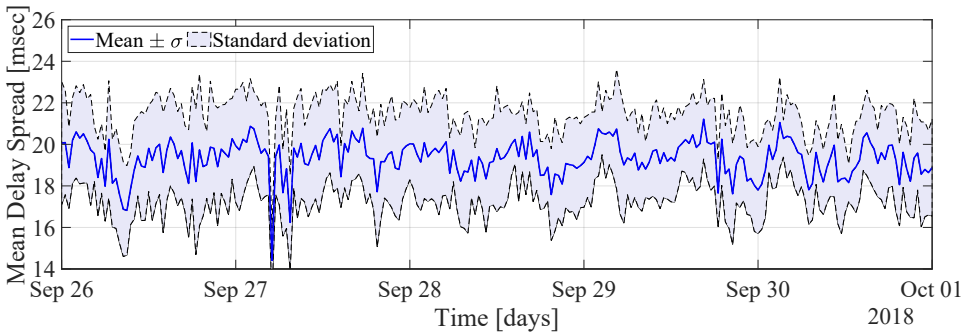

(a) AMAR-A

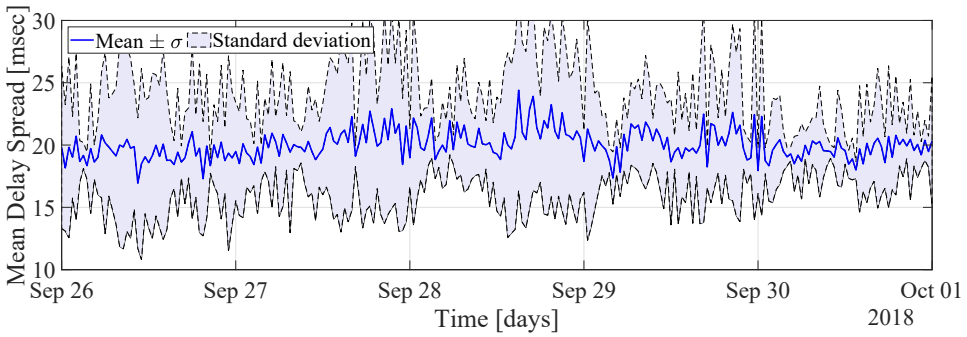

(b) AMAR-B

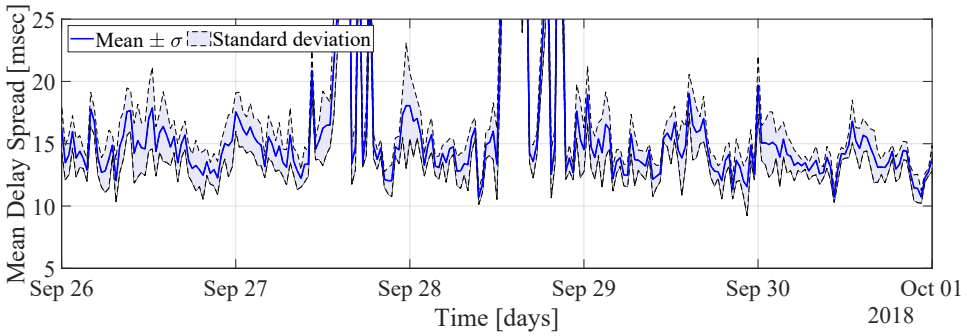

(c) AMAR-C

Figure 5.4: Statistical delay spread over five days from nine LFM up signals and 10 LFM down signals.

As can be observed, the mean delay spread varies around 18 ms, for AMAR-A and AMAR-B, and 16 ms for AMAR-C, which agrees with the simulation results reported in Chapter 4, Section 4.2. It should be noted that the delay spread for AMAR-C range has a few outliers, and this is attributed to the fact that the channel gain of the main path drops significantly, such that the noise at the output of the CIR estimate is mis-interpreted as additional path delays.

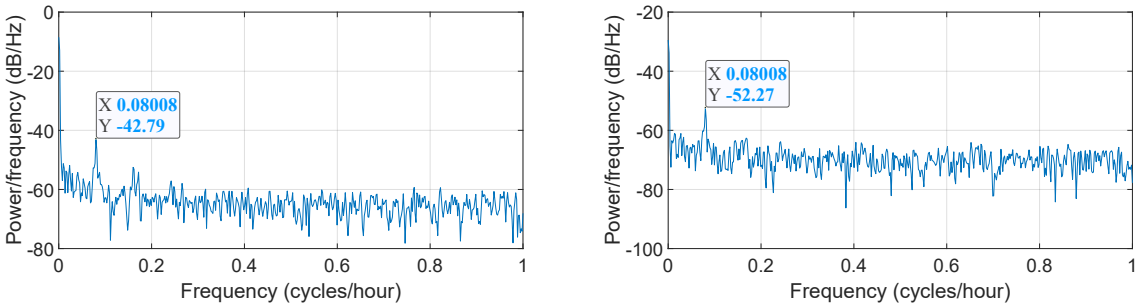

(a) Mean delay spread

(b) Delay spread standard deviation

Figure 5.5: Power spectral density on the mean and variance of the delay spread for AMAR-A.

As shown in Figures 5.5a, and 5.5b, the mean and standard deviation of the delay spread has a characteristic frequency at the tide cycle near 1/12.5 cycles per hour.

Following this, the mean delay spread was also plotted against the tide level. This is depicted in Figures 5.6a, 5.6b, and 5.6c. AMAR-A also shows an increasing trend in the delay spread. For AMAR-B, an increasing trend in the mean delay spread is evident. This indicates the mean delay spread is larger at high tides and agrees with the delay spread model in Chapter 4. However in AMAR-C, a more parabolic trend is evident. The next section will discuss the effect of flow on the time of arrival of the signal.

5.3 LOS and Surface Bounce Propagation Delay

In this section, a statistical analysis on the effect of mean and turbulent flow on the propagation delay of the LOS signal is provided. To obtain the propagation delay, the received signal is cross-correlated with a reference signal, decimated, and the propagation delay of the signal from the previous transmission, 30 minutes earlier, is subtracted to eliminate the clock drift. Note that for this analysis AMAR-A is used to ensure that the LOS can be easily separated from the surface bounce. The LOS and surface bounce propagation delays are separate peaks within the cross-correlated signal. Statistics are then calculated on the 19 propagation delays every 30 minutes, including the mean and standard deviation.

Figure 5.7 shows the LOS and a single surface bounce mean propagation delay over 14 days. Both the LOS and surface bounce mean propagation delays follow the trend of the mean flow velocity showing the effect of advection. The longer path length should result

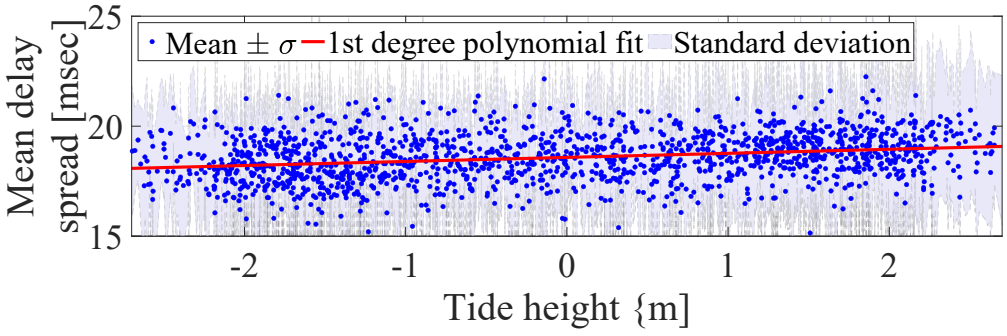

(a) AMAR-A

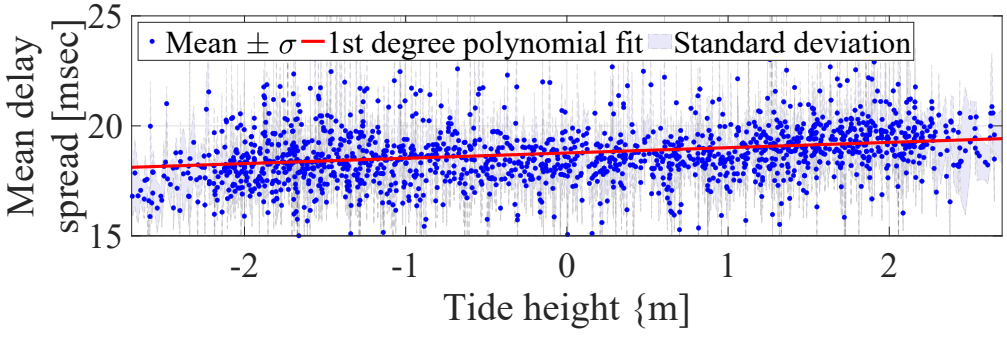

(b) AMAR-B

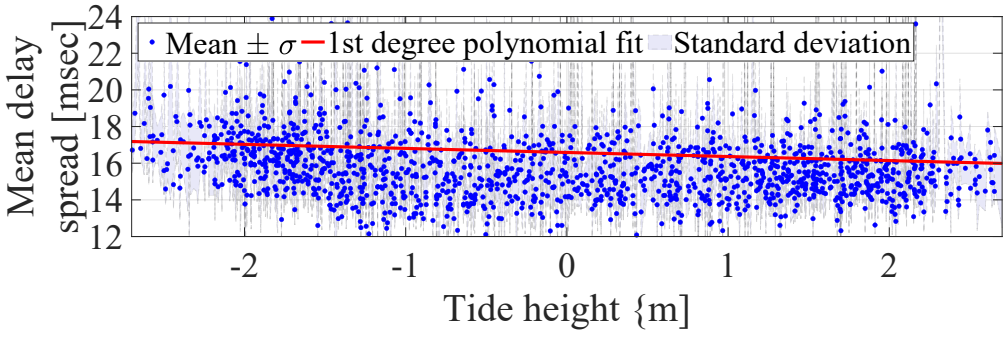

(c) AMAR-C

Figure 5.6: Statistical channel gain over five days from nine up signals and 10 down signals.

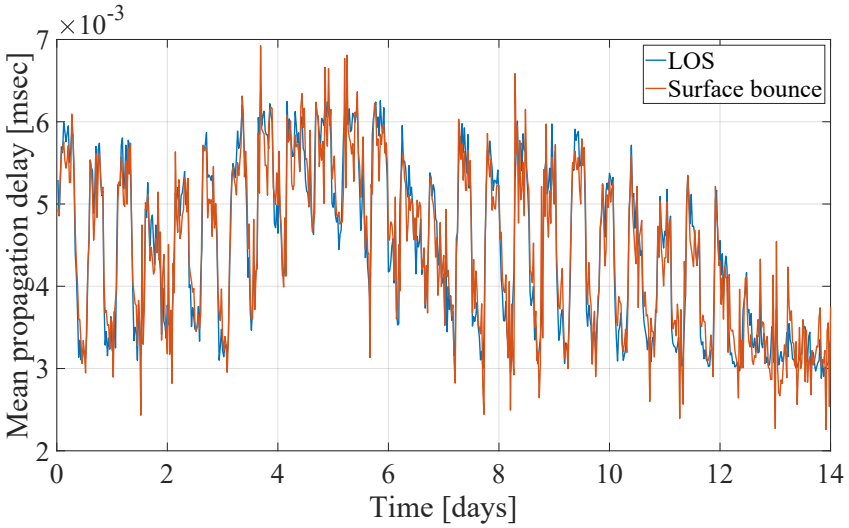

Figure 5.7: Time of arrival mean value as a function of time at AMAR-A.

in the 9.4 msec time difference between the LOS and SB arrivals, shown in Table 3.3. The difference between the maximum and minimum propagation delay for a given cycle is larger for the SB path where it is exposed to the effects of advection for a longer period.

Figure 5.8a and Figure 5.8b show the LOS and the single surface bounce propagation delay standard deviation respectively over 14 days. The propagation delay standard deviation jumps when the flow velocity is negative and has recently changed direction. Note that this is only at the beginning of the new tide and once the flow reaches the maximum, the propagation delay decreases again. This is evidence that the sea surface roughness are responsible for the higher standard deviation of the propagation delays. The surface bounce propagation delay standard deviation is approximately two magnitudes higher than the LOS propagation delay standard deviation.

For both the LOS and surface bounce, the mean value of the propagation delay varies with the flow speed; however, only the standard deviation of the surface bounce propagation delay varies with the flow. The LOS propagation delay standard deviation is approximately equal to 8 μsec at the limit of time resolution of the system, as defined in Section 3.1.1. The result shows that the statistical propagation delay model of flow with low turbulence does not accurately predict the LOS propagation delay physical behaviour.

A PSD of the LOS propagation delay standard deviation is shown in Figure 5.9a. As

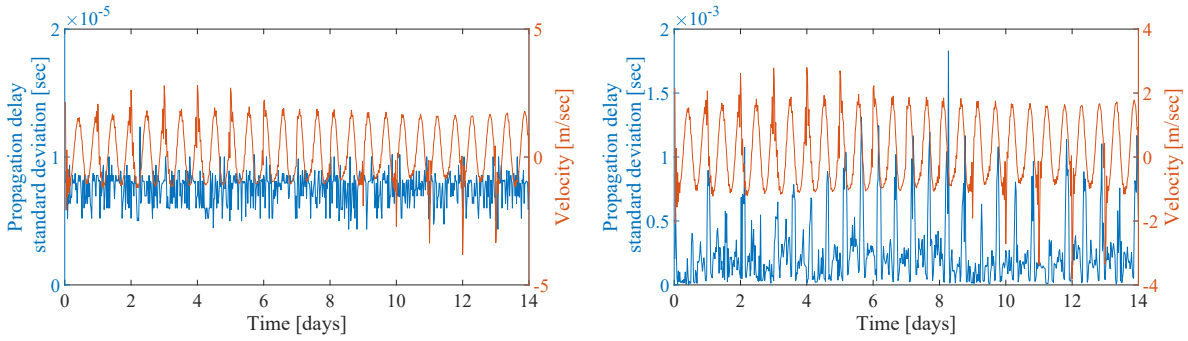

(a) Line of Sight (b) Surface Bounce

Figure 5.8: Comparison of the propagation delay standard deviation for the LOS path and for the surface reflection for AMAR-A.

previously mentioned, there were small spikes in the LOS propagation delay standard deviation apparent in Figure 5.8a; however, it is not shown above the noise floor in the PSD. Following this, a PSD of the surface bounce propagation delay standard deviation has a strong peak at 1/12.5 cycles per hour which confirms that it has a similar period to the semi-diurnal tide cycle as seen in Figure 5.9b. Interestingly, there are also strong peaks in the PSD of this signal for periods of approximately six hours and 3.5 hours near harmonics of the semi-diurnal tidal frequency. The analysis of these statistics provides an indication that the flow impacts the measured channel characteristics including the transmission loss and the delay profile, with a strong contribution to the variability by the surface bounce.

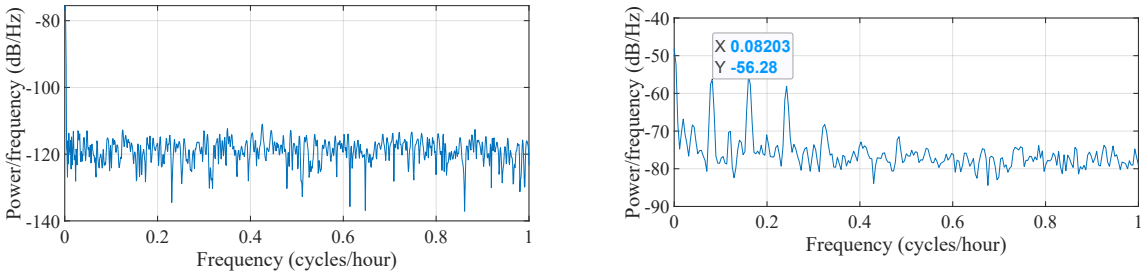

(a) LOS (b) Surface Bounce

Figure 5.9: Comparison of the PSD of the propagation delay standard deviation for the LOS path and for the surface reflection for AMAR-A.

To confirm the effect of the the variations in the environmental conditions on the overall channel statistics, the probability distribution functions (PDF) of the measured data at low tide and high tide are shown in Figure 5.10 and compared to that of the stochastic model. It can be observed that the statistical properties are relatively close to those obtained using

the stochastic model. The mean and variance of the channel gain are lower than the model predicts. The mean delay spread values are higher than the statistical values, where as the variance is significantly smaller as compared to the model, especially at high tide.

Note that both the measured channel gain, and delay spread standard deviations are smaller than the simulated standard deviations reported in Chapter 4, Section 4.2. This is attributed to the fact that the accuracy was limited by the background noise. Because of the idealized surface and bottom boundaries, Bellhop tends to over estimate the contribution of the reflected paths.

These measurement results of the channel impulse response confirm that the physical phenomena that accompany the tide, i.e the water depth, the mean flow and the turbulence have a significant impact on the channel conditions. The following section will analyze the Doppler spread in the presences of the tides.

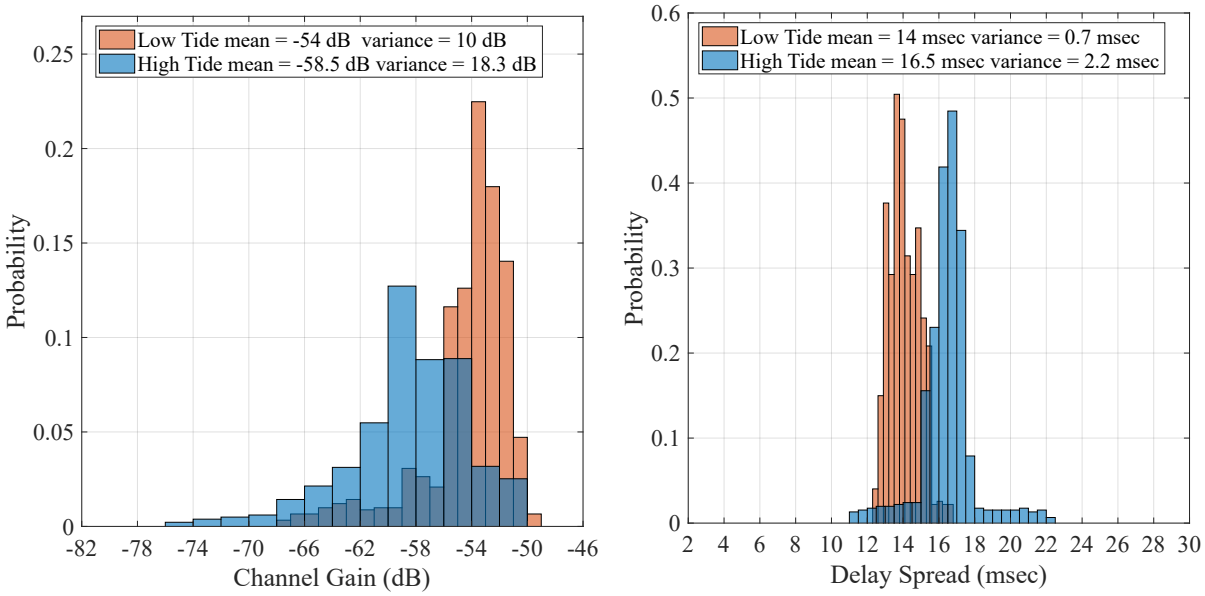

Figure 5.10: Probability distribution function of the measured channel gain and delay spread on Sep. 28th, 2018.

5.4 Chapter 5 Summary

This chapter covered the effects of flow and turbulence of the data obtained from the Grand Passage experiment conducted from late September through to the end of October 2018. In the experiment there was an acoustic source that transmitted a programmed signal consisting

of linear frequency up and down sweeps, and tones at four different frequencies. This signal was sent to AMARs that were each equipped with four omni-directional hydrophones.

In the data analysis, the channel gain, and RMS delay spread were analyzed, and a statistical analysis was then performed on the results. Before the channel gain and RMS delay spread were analyzed, the clock drift of the programmed acoustic signal, over all the days, had to be solved. The solution was to synchronize to the first LFM up signal on each transmission, and then determine the arrival of the other signals from there. The channel gain for all the LFM sweeps was calculated. The channel gain, and RMS delay spread vary over the days as the tide height changes.

Following up on this, the statistical analysis also showed that the channel gain and the RMS delay spread varied with the tide heights. It appears the tide cycle and mean and turbulent flow have a relationship with the Doppler shift, Doppler spread, the channel gain and the RMS delay spread.

A comparison was conducted between the LOS and surface bounce propagation delay. Results show that the mean propagation delay for the LOS, and surface bounce, both have a fundamental frequency at the tide cycle and follow the direction of the flow. The LOS and surface bounce variability however, have different orders of magnitude. The LOS arrival variability does not seem to be affected by the tidal cycle and the flow. This could be due to the result of limited time resolution of the experimental set up. The surface bounce propagation delay variability has a fundamental frequency at the same tidal cycle. This could be due to waves formed consistently and regularly during the beginning of the flood tide. Specifically the standard deviation of the propagation delay increases with flow, which indicates that the time varying flow has an impact in how the propagation delay of the surface bounce varies on the small time scale.

Chapter 6

Conclusion

In this Chapter, a conclusion will be presented. Specifically; in Section 6.1, the summary of contributions will be discussed, then in Section 6.2, the future work will be addressed.

The channel characteristics such as transmission loss, delay spread, propagation delay and Doppler spread were affected from a periodic cycle with the same frequency as the tidal cycle; however, the question that remains is what the actual physical phenomena is that creates this. Is it turbulence, mean flow, or surface roughness? The data gives us insight as to what this reason is. Second, the simulations indicate that turbulence can have an impact on the propagation delay variability. Higher mean flow results in larger turbulence with a predicted increase in the propagation delay variability. The correlation length scale of the turbulence along the propagation path also determines the scale of the propagation delay variability, where larger turbulence leads to larger variability. In addition, the surface bounce path has more of an impact on the arrival time variability as compared to the LOS path. This is most likely due to the surface roughness producing a variability that is several orders of magnitude larger. Finally, the model indicated that the mean flow and turbulence has an effect on the LOS time varying latency; however, this was not evident in the actual data. This discrepancy may be due to an issue with the model or the effect is too minimal to be detected.

6.1 Summary of Contributions

In this work, the effect of flow, changing channel depth and turbulence on the acoustic propagation channel are carefully analyzed. A simulation relying on ray-tracing with varying sound speed as a function of range and depth is configured to model the effect of the mean and turbulent flow on the acoustic channel. To model various turbulent scales, the sound speed as a function of range was evaluated with varying degrees of correlation as a function of space. It is confirmed that turbulence has an important impact on the time of arrival variability and it is shown how the turbulence degree of correlation (inversely related to the

decay factor) can provide a variance of the LOS propagation delay that is on the same order of magnitude as the measurements. Specifically, for the short range scenario a standard deviation on the order of 10 microseconds is obtained for alpha is equal to 100 at high flow. To validate the model, a sea trial was undertaken in the Bay of Fundy with the propagation channel parallel to the direction of flow. A maximum flow speed of 2.5 meters per second is measured using an ADCP. It is clearly observed that the variation in transmission loss amplitude, the Doppler spread, and the delay spread were all affected from a periodic cycle with the same frequency as the tidal cycle. By carefully analyzing the variation of the direct LOS time of arrival in comparison to that of the surface bounce, it is clear that the surface bounce has a larger propagation delay variability than the direct LOS. This can be attributed to the fact that there is very low turbulence in the direct LOS, while, as the signal propagates through the water column, and bounces off the surface, it is subject to different phenomena that vary quickly with time, including the surface roughness.

6.2 Future Work

Future work on the effect of flow on the channel characteristics includes improving the procedure for the data analysis and the turbulence modelling. The current data analysis procedure provides accurate channel characteristics; however, significant deep fading in the processed signal still exists in the plots. Perhaps a better filtering procedure could be used to filter out deep fades, that are most likely caused by significant noise. Another suggestion is to conduct the experiment in a high tidal environment absent of a ferry in close proximity, as the noise generated may skew the results.

The current turbulence model uses the Bellhop simulator to compute theoretical arrival times given the environmental inputs. The turbulence model uses a random Gaussian distribution to model large and small turbulent regions in the range dependent SSPs. The decay coefficient α is used to produce these large and small regions. The distributions are around an assumed sound speed at all depths of 1480 meters per second. The modelling of the turbulence could be improved by consulting publications that report direct measurements of turbulence in tidal channels [44].

Further in depth simulations on the channel gain, delay spread, Doppler spread, and propagation delay could provide more insight than current simulations. Current results do indicate that high-flow and turbulent environments have a large impact on the channel

characteristics. Further analysis into environmental factors that could influence the data is recommended. Interferences such as the impact of the ferry transiting the test site, and other environmental factors such as sediment generated noise [45] should be investigated.

Bibliography

[1] M. Stojanovic and P-P J. Beaujean, "Acoustic communication," in *Springer Handbook of Ocean Engineering*, Manhar R. Dhanak and Nikolaos I. Xiros, Eds., pp. 359–386. Springer International Publishing, Cham, 2016.

[2] Canadian Seabed Research Ltd., "Seabed analysis for tidal energy development Grand Passage, Petit Passage, and Digby Gut, Digby County, Nova Scotia. Contract report prepared by Seabed Research for Fundy Tidal Inc., CSR Report # 13167.," 2014.

[3] "The Global Fishing Industry - FISHER Project," [Online]. Available: `https://www.fisherproject.org/the-global-fishing-industry`, [Accessed: 29-Sept.-2021].

[4] National Oceanic and Atmospheric Administration, "Why should we care about the ocean?," [Online]. Available: `https://oceanservice.noaa.gov/facts/why-care-about-ocean.html`, [Accessed:24-Sept.-2021].

[5] H. Davor, "Ocean Energy," [Online]. Available: `https://www.our-energy.com/ocean-energy.html`, [Accessed: 21-Sept.-2021].

[6] M. J. Woo, "Tidel Energy: The New Sustainable Resource," [Online]. Available: `https://www.woodharbinger.com/tidal-energy-sustainable-resource`, [Accessed: 23-Sept.-2021].

[7] Ocean Power Technologies, "Home," [Online]. Available: `https://oceanpowertechnologies.com/`, [Accessed: 15-Sept.-2021].

[8] R. Karsten, J. Culina, A. Swan, M. O'Flaherty-Sproul, A. Corkum, D. Greenberg, and M. Tarbotton, "Assessment of the Potential of Tidal Power from Minas Passage and Minas Basin prepared for Offshore Energy Research Association," November 2011.

[9] J. H. Steele, S. A. Thorpe, and K. K. Turekian, *Encyclopedia of Ocean Sciences 2nd Ed.*, Academic Press, 2009.

[10] "Teledyne Benthos," [Online]. Available: `http://www.benthos.com/acoustic-telesonar-modem-atm-910-series`, [Accessed: 14-Sept.-2021].

[11] "Acoustic Communications Group," [Online]. Available: `http://acomms.whoi.edu/`, [Accessed: 12-Sept.-2021].

[12] "LinkQuest Underwater Acoustic Modems," [Online]. Available: `http://www.link-quest.com/html/uwm1000.htm`, [Accessed: 16-Sept.-2021].

[13] "Acoustic Modems — EvoLogics," [Online]. Available: `http://www.evologics.de/acoustic-modem`, [Accessed: 17-Sept.-2021].

[14] "Acoustic Communications," [Online]. Available: http://www.sercel.com/Products/seabed/underwateracoustics/mats$_$3g.php, [Accessed: 19-Sept.-2021].

[15] "Micron Modem — Tritech — Outstanding Performance in Underwater ...," [Online]. Available: http://www.tritech.co.uk/product/micron-data-modem, [Accessed: 14-Sept.-2021].

[16] A. A. Syed and J. Heidemann, "Time synchronization for high latency acoustic networks," in *Proceedings IEEE INFOCOM 2006. 25TH IEEE International Conference on Computer Communications*, 2006, pp. 1–12.

[17] G. Qiao, Z. Babar, L. Ma, S. Liu, and J. Wu, "Mimo-ofdm underwater acoustic communication systems—a review," *Physical Communication*, vol. 23, pp. 56–64, 2017.

[18] G. Leus and P. A. van Walree, "Multiband OFDM for Covert Acoustic Communications," *IEEE Journal on Selected Areas in Communications*, vol. 26, no. 9, pp. 1662–1673, 2008.

[19] H. R. Mirhedayati and J-F. Bousquet, "A Time-Varying Filter for Doppler Compensation Applied to Underwater Acoustic OFDM," *Sensors (Basel, Switzerland)*, vol. 19, no. 1, pp. 105, 2018.

[20] M. Stojanovic, "Efficient processing of acoustic signals for high-rate information transmission over sparse underwater channels," *Physical Communication*, vol. 1, no. 2, pp. 146–161, 2008.

[21] P. Qarabaqi and M. Stojanovic, "Statistical characterization and computationally efficient modeling of a class of underwater acoustic communication channels," *IEEE Journal of Oceanic Engineering*, vol. 38, no. 4, pp. 701–717, 2013.

[22] M. Benedini and G. Tsakiris, *Water quality modelling for rivers and streams*, vol. 70, Springer Netherlands, 2013.

[23] J. McMillan, *Turbulence Measurements in a High Reynolds Number Tidal Channel*, Ph.D. thesis, Dalhousie University, 2017.

[24] P. Augier, A. V. Mohanan, and E. Lindborg, "Shallow water wave turbulence," *Journal of Fluid Mechanics*, vol. 874, pp. 1169–1196, 2019.

[25] D. R. Barclay, "Passive Acoustic Monitoring in Tidal Channels and High Flow Environments. OERA-The Pathway Program," p. 2, 2019.

[26] C. Bassett, J. Thomson, P. H. Dahl, and B. Polagye, "Flow-noise and turbulence in two tidal channels," *The Journal of the Acoustical Society of America*, vol. 135, no. 4, pp. 1764–1774, 2014.

[27] L. Dong and H. Dong, "Bellhop – A modeling approach to Sound propagation in the ocean," 2014.

[28] F. B. Jensen, W. A. Kuperman, M. B. Porter, and H. Schmidt, *Computational Ocean Acoustics*, Springer Publishing Company, Incorporated, 2nd edition, 2011.

[29] P. Qarabaqi and M. Stojanovic, "Statistical Characterization and Computationally Efficient Modeling of a Class of Underwater Acoustic Communication Channels," *IEEE Journal of Oceanic Engineering*, vol. 38, no. 4, pp. 701–717, Oct 2013.

[30] J. Rudander, T. Husy, P. Orten, and P. van Walree, "Shallow-water channel sounding for high speed acoustic communication," in *OCEANS 2017 - Aberdeen*, 2017, pp. 1–8.

[31] R. J. Urick, *Propagation of sound in the sea: transmission loss, I*, Peninsula Pub., 1996.

[32] D. Tse and P. Viswanath, *Fundamentals of wireless communication*, Cambridge, 2013.

[33] E. I. Thorsos, "The validity of the Kirchhoff approximation for rough surface scattering using a Gaussian roughness spectrum," *The Journal of the Acoustical Society of America*, vol. 83, no. 1, pp. 78–92, 1988.

[34] S. A. Thorpe, *An introduction to ocean turbulence*, Cambridge University Press, 2007.

[35] R. J. Urick, *Ambient noise in the sea*, Peninsula Publishing, 1986.

[36] L. Bjørnø, T. Neighbors, and D. Bradley, *Applied Underwater Acoustics*, Elsevier, 2017.

[37] "Acoustic Doppler Current Profiler," [Online]. Available: `https://www.oceanscan.net/p-RDI_DOPPLER_260l`, [Accessed: 19-Sept.-2021].

[38] "Autonomous Multichannel Acousitc Recorders," [Online]. Available: `https://www.jasco.com/`, [Accessed: 16-Sept.-2021].

[39] Z. Dou, W.D. Song, and W.X. Zhang, "Study on the Characteristics of LFM Signals, BC Signals and Their Mixed Modulation Signals," *Int. J. Communications, Network and System Sciences*, vol. 10, pp. 196–205.

[40] MathWorks, "Periodogram power spectral density estimate," [Online]. Available: `https://www.mathworks.com/help/signal/ref/periodogram.html`, [Accessed: 19-Sept.-2021].

[41] MathWorks, "Welch's power spectral density estimate," [Online]. Available: `https://www.mathworks.com/help/signal/ref/pwelch.html`, [Accessed: 19-Sept.-2021].

[42] OSU TPXO Tide Models, "TPXO9-atlas," [Online]. Available: `https://www.tpxo.net/global/tpxo9-atlas`, [Accessed: 28-Sept.-2021].

[43] H. Ghannadrezaii, J. MacDonald, J-F Bousquet, and D. Barclay, "Channel Quality Prediction for Adaptive Underwater Acoustic Communication," in *2021 Fifth Underwater Communications and Networking Conference (UComms)*, 2021, pp. 1–5.

[44] M. Guerra, A.E. Hay, R. Karsten, G. Trowse, and R.A. Cheel, "Turbulent flow mapping in a high-flow tidal channel using mobile acoustic Doppler current profilers," *Renewable Energy*, vol. 177, pp. 759–772.

[45] A. R Lombardi, A. E. Hay, and D. R. Barclay, "Soundscape characterization in a dynamic acoustic environment: Grand Passage, Nova Scotia, a planned in-stream tidal energy site. In Proceedings of Meetings on Acoustics 4ENAL ," *Acoustical Society of America.*, vol. 27, no. 1, pp. 005001, July 2016.